# Reactive Transport Modelling Investigation of Elevated Dissolved Sulphide Concentrations in Sedimentary Basin Rocks

**NWMO-TR-2018-07**                                        **August 2018**

**Mingliang Xie[1], Danyang Su[1], K. Ulrich Mayer[1] and**

**Kerry T. B. MacQuarrie[2]**

[1]Department of Earth, Ocean and Atmospheric Sciences, University of British Columbia
[2]Department of Civil Engineering, University of New Brunswick

nwmo

NUCLEAR WASTE       SOCIÉTÉ DE GESTION
MANAGEMENT          DES DÉCHETS
ORGANIZATION        NUCLÉAIRES

# Reactive Transport Modelling Investigation of Elevated Dissolved Sulphide Concentrations in Sedimentary Basin Rocks

## NWMO-TR-2018-07

August 2018

**Mingliang Xie[1], Danyang Su[1], K. Ulrich Mayer[1] and Kerry T. B. MacQuarrie[2]**
[1]Department of Earth, Ocean and Atmospheric Sciences, University of British Columbia
[2]Department of Civil Engineering, University of New Brunswick

## Document History

| Title: | Reactive Transport Modelling Investigation of Elevated Dissolved Sulphide Concentrations in Sedimentary Basin Rocks | | |
|---|---|---|---|
| Report Number: | NWMO-TR-2018-07 | | |
| Revision: | R000 | Date: | August 2018 |
| [1]Department of Earth, Ocean and Atmospheric Sciences, University of British Columbia [2]Department of Civil Engineering, University of New Brunswick | | | |
| Authored by: | Mingliang Xie[1], Danyang Su[1] | | |
| Verified by: | Kerry T. B. MacQuarrie[2] | | |
| Approved by: | K. Ulrich Mayer[1] | | |
| Nuclear Waste Management Organization | | | |
| Reviewed by: | Tammy Yang, Mark Jensen, Monique Hobbs | | |
| Accepted by: | Paul Gierszewski | | |

# ABSTRACT

**Title:**        **Reactive Transport Modelling Investigation of Elevated Dissolved Sulphide Concentrations in Sedimentary Basin Rocks**

**Report No.:**   **NWMO-TR-2018-07**

**Author(s):**    Mingliang Xie[1], Danyang Su[1], K. Ulrich Mayer[1] and Kerry T. B. MacQuarrie[2]

**Company:**      [1]Department of Earth, Ocean and Atmospheric Sciences, University of British Columbia

[2]Department of Civil Engineering, University of New Brunswick

**Date:**         August 2018

**Abstract**

Groundwater with total dissolved sulphide concentrations in excess of $1.0 \times 10^{-4}$ mol $L^{-1}$ is relatively common at intermediate depths in sedimentary basins, including regions of the Michigan Basin in southeastern Ontario. However, the mechanisms responsible for the formation and distribution of these brackish sulphidic waters are not fully understood. Anaerobic microbial sulphate reduction is a common process resulting in the formation of sulphide. Sulphate reduction rates depend on many factors including the concentration of sulphate, the abundance of organic substances, redox conditions, salinity and the species of sulphate reducing bacteria (SRB). A new conceptual model considering the effect of salinity on the rate of sulphate reduction was developed and implemented in MIN3P-THCm. Generic 2D modelling investigations were undertaken to provide a potential explanation for the presence of observed sulphidic waters and their distribution in the Michigan Basin. Simulated sulphide concentrations are of the same order of magnitude as observational data in southern Ontario and the model was able to generally reproduce the depth-dependent distribution of sulphide.

# TABLE OF CONTENTS

## LIST OF TABLES

## <u>LIST OF FIGURES</u>

## 1. INTRODUCTION

Sulphur water, which commonly refers to groundwater having an unpleasant 'rotten egg' smell, is often associated with a threshold dissolved concentration of 0.05 mg $L^{-1}$ ($1.4 \times 10^{-6}$ mol $L^{-1}$) as hydrogen sulphide (OME 2006).  Sulphidic groundwater (SUL), containing total dissolved sulphide in excess of $1.0 \times 10^{-4}$ mol $L^{-1}$, is commonly found at intermediate depths in sedimentary basin rocks in southeastern Ontario as indicated in Figure 1 and  Figure 2 (Carter 2012, Carter et al. 2015).  Conversely, at deeper and shallower depths, relatively low total dissolved sulphide concentrations have been reported.  The mechanisms responsible for the formation of these sulphidic waters in southern Ontario are not fully understood.  Anaerobic microbial sulphate reduction is a common process resulting in the formation of sulphidic waters and has been intensively investigated in various fields of environmental engineering (Brown 1982) and by the oil and gas industry (Tang et al. 2009).  Sulphate reduction rates depend on many factors including the concentration of sulphate, the abundance of organic substances, redox conditions, temperature, salinity and the species of sulphate reducing bacteria (SRB) (Brandt et al. 2001, Foti et al. 2007).  Generally, the activity of SRB is strongly suppressed if the salinity of the fluid is very high (Oren 1999), which at least in part explains the co-existence of sulphate and organic matter in the reducing environment of deep sedimentary rocks in southern Ontario (Hobbs et al. 2011).  In the Michigan Basin saline waters and brines (SAL in Figure 1) dominate at depth, whereas fresh water (FRE) exists near the surface.  Therefore, it is reasonable to hypothesize that highly saline waters in the deeper parts of the basin, and unsuitable redox conditions near the ground surface, suppress the activity of SRB in these regions.
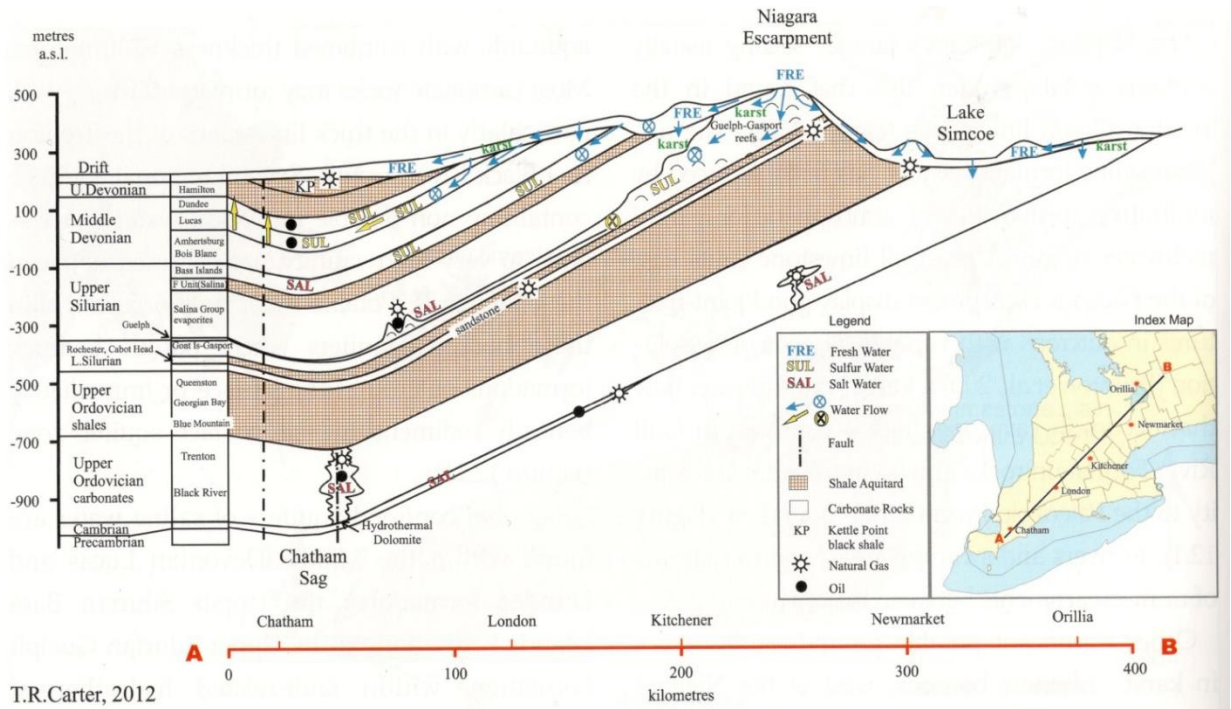
**Figure 1: Conceptual Model and Observed Distribution of Sulphidic Water (SUL) at the Eastern Flank of the Michigan Basin (Carter 2012)**
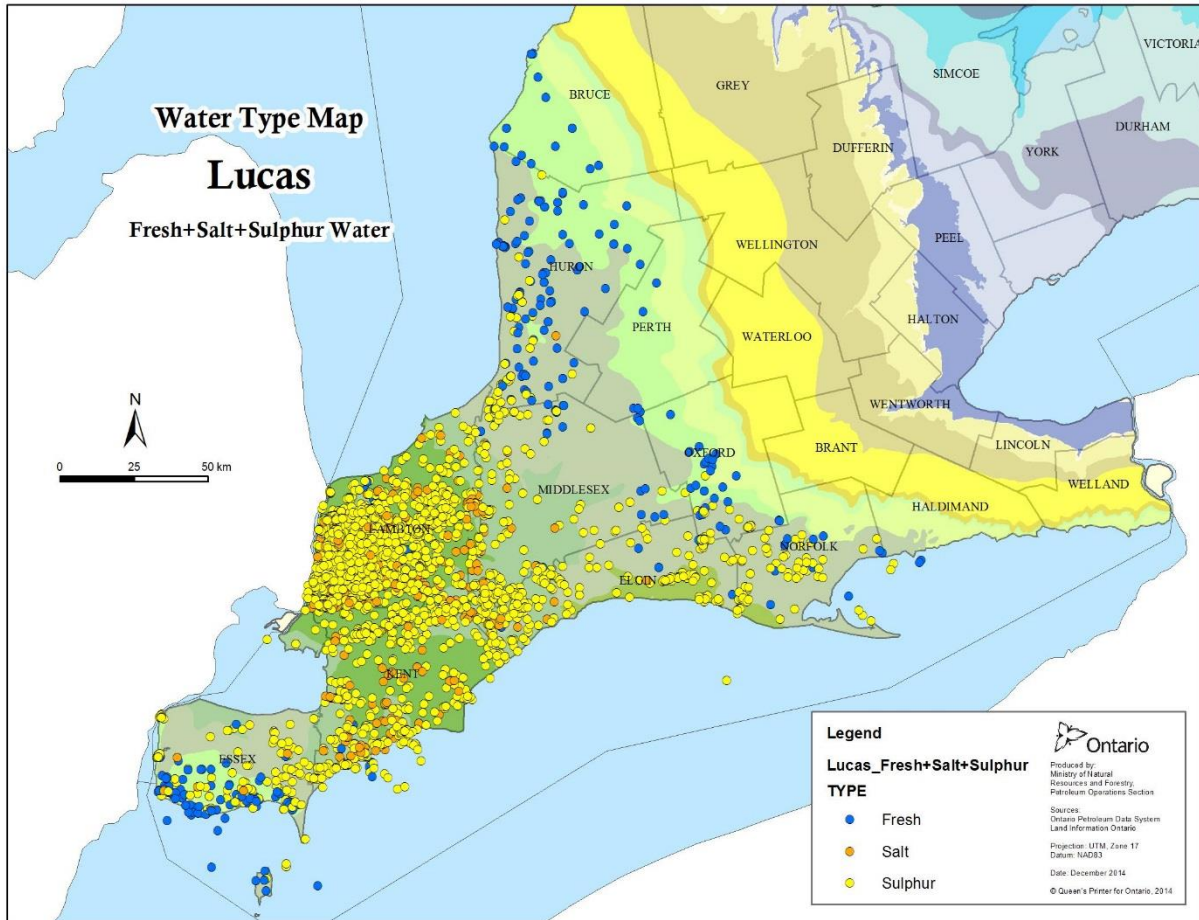
**Figure 2: Water Type Map in the Lucas Formation in Southern Ontario (Carter et al. 2015)**

Carter et al. (2015) published a set of maps showing the distribution of sulphidic groundwaters in southern Ontario based on groundwater chemistry data reported by companies drilling either shallow irrigation wells or deep petroleum wells (Figure 2). Based on this data set vertical distributions of chloride, sulphate, and sulphide are presented in Figure 3. Samples with elevated sulphide concentrations (ranging from $5.0 \times 10^{-5}$ to $1.5 \times 10^{-3}$ mol L$^{-1}$) were collected at depths between 50 and 140 m (Figure 3 right), with the highest observed sulphide concentrations approaching $2 \times 10^{-3}$ mol L$^{-1}$ at a depth of around 100 m (Figure 3 right). At greater depths (> 400 m), sulphide concentrations were lower (ranging from $6.0 \times 10^{-6}$ to $7.0 \times 10^{-5}$ mol L$^{-1}$). The data also show that higher sulphide concentrations were observed in samples with relatively low salinity (or Cl$^{-}$ concentration) (Figure 4). At depths exceeding 400 m the concentration of Cl$^{-}$ is substantial (typically ranging between 4 and 9 mol L$^{-1}$). These observations are consistent with experimental findings, which have demonstrated that salinities greater than 130 g L$^{-1}$ inhibit salt water strains of Desulphovibrio desulphuricans, while salinities up to approximately 260 g L$^{-1}$ inhibit the activity of extremely salt-tolerant species of SRB (Littlewood and Postgate 1957; Oren 1999; Brandt et al. 2001; Foti et al. 2007). In groundwaters with lower salinity (< 40 g L$^{-1}$) and lower Cl$^{-}$ concentrations (< 1.0 mol L$^{-1}$),

sulphide concentrations were more scattered, but often showed more elevated concentrations (ranging from $6.0{\times}10^{-7}$ to $1.8{\times}10^{-3}$ mol L$^{-1}$) (Figure 4).

Figure 3 shows that the concentration of sulphate is relatively uniformly distributed vertically, with concentrations near $2{\times}10^{-3}$ mol L$^{-1}$, at depths greater than 800 m.  Sulphate concentrations span from $1.0{\times}10^{-3}$ to $2.0{\times}10^{-2}$ mol L$^{-1}$ at depths between 400 and 800 m, and from $2.0{\times}10^{-5}$ to $2.0{\times}10^{-2}$ mol L$^{-1}$ at depths between 0 and 400 m (Figure 3).  Sulphate is relatively common within these rock sequences and thus available for biogenic sulphate reduction.
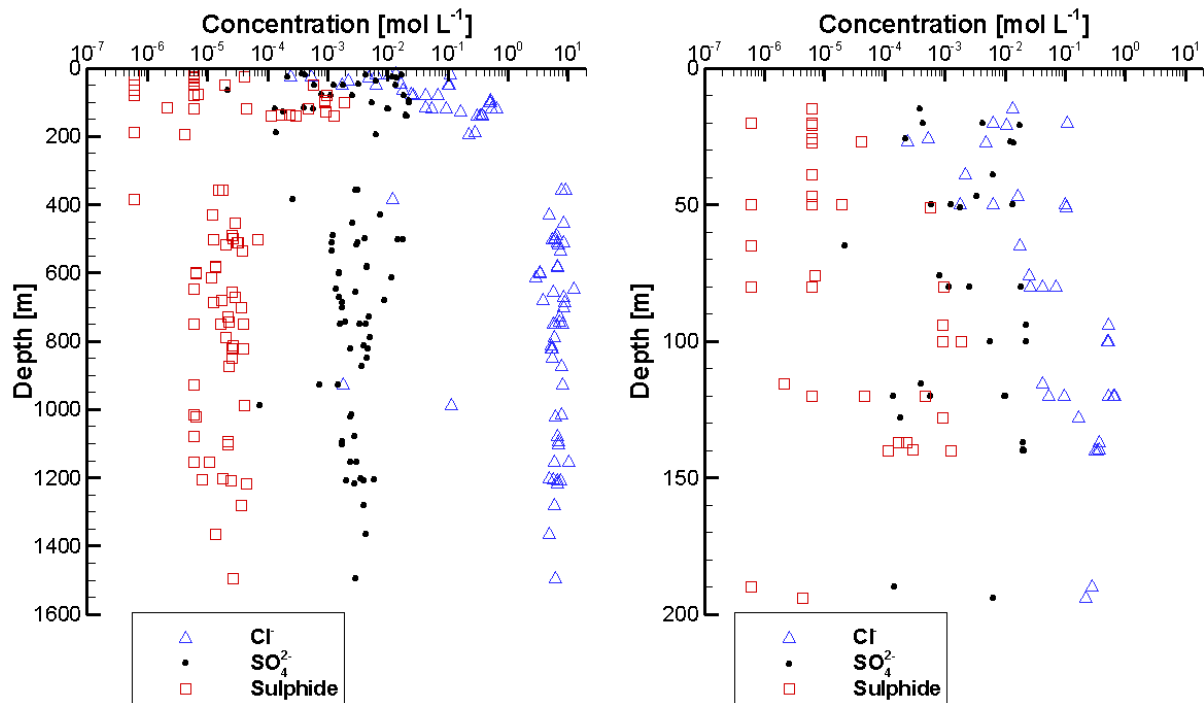


**Figure 3: Measured Chloride, Sulphate and Sulphide Concentrations (in mol L$^{-1}$) vs Sampling Depth.  Left – Overview; Right – Detailed View from 0 to 200 m Depth (Based on Data Presented by Carter et al. 2015)**
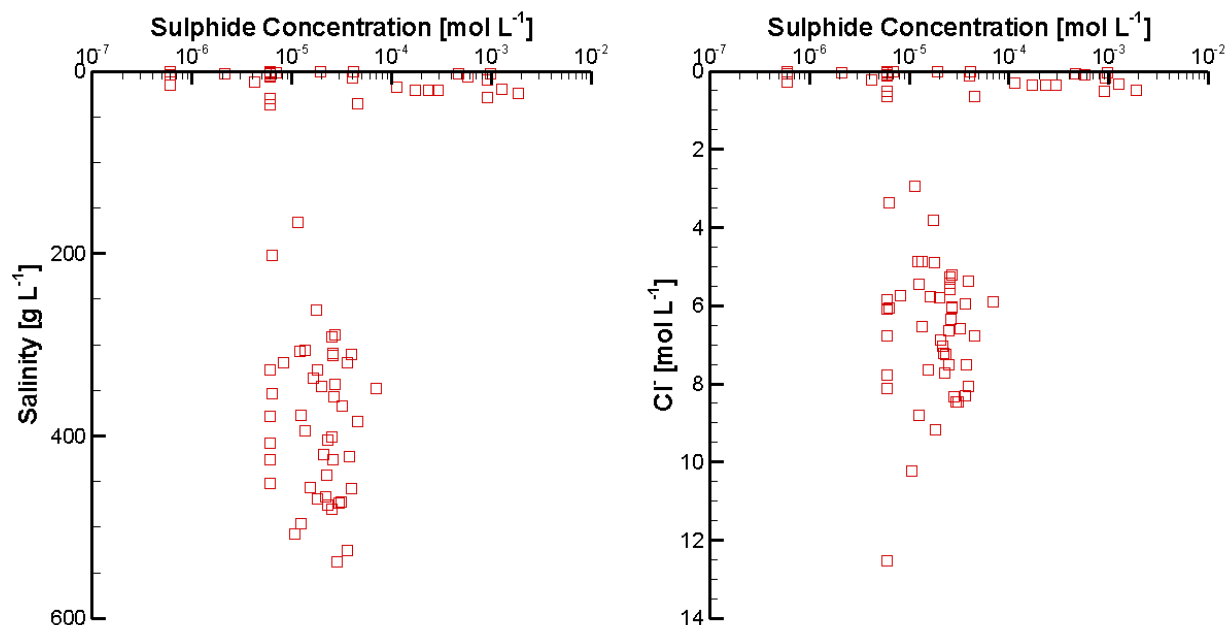
**Figure 4: Observed Sulphide Concentrations vs the Salinity (Left) and vs. Total Cl⁻ Concentrations (Right) (Based on Data Presented by Carter et al. 2015)**

This report investigates processes potentially controlling the formation and distribution of sulphidic waters in a generic sedimentary basin using the reactive transport simulator MIN3P-THCm (v1.0.524). The objective of this work is to develop plausible explanations for the formation and observed distribution of sulphidic waters and to delineate the controlling factors. The data set presented by Carter et al. (2015) is used to develop the conceptual reactive-transport framework and for assisting with interpreting the simulation results.

## 2.  MODEL FORMULATION AND DEVELOPMENT

MIN3P-THCm (v1.0.524) was developed on the basis of the original MIN3P code (Mayer 1999; Mayer et al. 2002) and further enhancements included in MIN3P-D (Henderson et al. 2009) and MIN3P-NWMO (Bea et al. 2011).  MIN3P-THCm is a general purpose multicomponent reactive transport code for variably saturated porous media.  It is characterized by a high degree of flexibility and is applicable to a wide range of hydrogeological and geochemical problems.  Chemical processes included are homogeneous reactions in the aqueous phase, as well as a variety of heterogeneous reactions.  The code can simulate groundwater flow, advective-diffusive solute transport, multicomponent diffusion and electrochemical migration following the approach of Giambalvo et al. (2002), multisite ion exchange and geochemical reactions under variable density, non-isothermal, and highly saline conditions (Bea et al. 2011; 2012; Xie et al. 2014a, 2014b).  The governing equations, with a focus on the new code developments, are summarized below.  For additional details on the general code capabilities, the reader is referred to Mayer et al. (2002), Henderson et al. (2009), Mayer and MacQuarrie (2010) and Bea et al. (2011).

## 2.1 SALINITY DEPENDENT SULPHATE REDUCTION (SDSR) MODEL

Biogenic sulphate reduction can generally be described by (Gibson et al. 2011):

$$CH_2O + 0.5\,SO_4^{2-} \rightarrow CO_3^{2-} + 0.5H_2S + H^+ \qquad \textbf{Equation 2-1}$$

in which $CH_2O$ represents organic substances present in the stratigraphic units as part of the solid phase. Numerically, this reaction can be treated in the same manner as mineral dissolution/precipitation reactions, and can be modelled as a kinetically-controlled, irreversible reaction. Experiments have demonstrated that many factors exert inhibition effects on hydrogen sulphide generation, such as the concentration of dissolved oxygen, accumulation of the reaction product hydrogen sulphide, and the salinity of the solution (Brandt et al. 2001; Brown 1982; Carter 2012; Tang et al. 2009). To take these factors into account, sulphate reduction is simulated using a simplified Monod-type rate expression of the form:

$$R = -k_{sal}k_{sulf}\left[\frac{[SO_4^{2-}]}{k_s + [SO_4^{2-}]}\right]\left[\frac{K_{HS^-}^{in}}{K_{HS^-}^{in} + [HS^-]}\right]\left[\frac{K_{O_2}^{in}}{K_{O_2}^{in} + [O_2(aq)]}\right] \qquad \textbf{Equation 2-2}$$

in which $R$ is the rate of sulphate reduction, $k_s$ is the half-saturation constant for sulphate, and $[SO_4^{2-}]$, $[HS^-]$ and $[O_2(aq)]$ represent the concentrations of sulphate, total aqueous sulphide (including $H_2S(aq)$ and $HS^-$ - which is applied to the description of all simulated results in this report) and dissolved oxygen, respectively. $K_{HS^-}^{in}$ and $K_{O_2}^{in}$ are the inhibition constants for total hydrogen sulphide and $O_2(aq)$, respectively. $k_{sulf}$ is the maximum rate constant of the biogenic sulphate reduction reaction and $k_{sal}$ is a salinity inhibition factor ranging from 0.0 to 1.0, which can be expressed as a function of salinity S [g/L] based on experimental data:

$$k_{sal} = f(S) \qquad \textbf{Equation 2-3}$$

Based on the groundwater chemistry data presented by Carter (2012), chloride is the dominant anion and is linearly correlated to salinity (Figure 5). Therefore, it is reasonable to express the salinity inhibition term as a function of Cl⁻ (see Equation 2-4 in Section 2.3.3). Alternatively, the salinity inhibition could be expressed directly as a function of *S* or as a function of Total Dissolved Solids (*TDS*); however, the latter approach has the disadvantage that it can lead to inhibition of sulphate reduction in groundwater with high sulphate concentrations, but relatively low concentrations of other major anions and cations, which would be incorrect.

Experimental data have shown that some SRB can survive under hypersaline conditions and tend to thrive within certain saline conditions depending on the background solution conditions (Foti et al. 2007; Brandt et al. 2001). The exact behaviour is dependent on the species of the SRB. However, detailed information on the species of SRB present in sedimentary rocks of southern Ontario is not available, and this factor has not been considered in the SDSR model presented here.
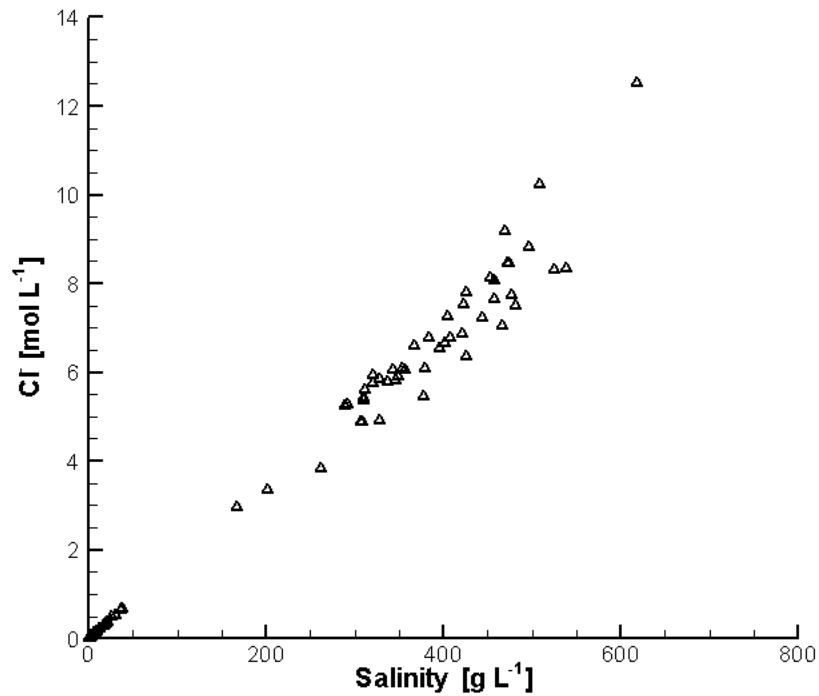
**Figure 5: Correlation of Salinity and Cl⁻ Concentration in Southern Ontario Groundwaters (Based on Data Presented by Carter et al. 2015)**

## 2.2   NUMERICAL IMPLEMENTATION AND SOLUTION STRATEGY

The governing equations are implemented using a finite volume technique for spatial discretization and implicit time weighting for the temporal discretization.  The reactive transport equations are solved using the global implicit approach, employing Newton's method for linearization (Mayer et al. 2002; Mayer and MacQuarrie 2010).

## 2.3   MODEL VERIFICATION

2.3.1 Problem Definition

This example verifies the salinity dependent sulphate reduction (SDSR) model through code comparison of MIN3P-THCm (v1.0.512) and PHREEQC v3.1.1.8288 (Parkhurst and Appelo 2013).

2.3.2 Model Setup

A 1D domain, 16.0 m in length, is discretized into 201 control volumes.  The domain is homogeneous and fully saturated, and contains calcite, anhydrite, halite and solid phase organic matter ($CH_2O$).  The initial hydraulic head is 0.0 m across the domain.  The hydraulic heads at the inflow and outflow boundaries are held constant at 1.4 m and 0.0 m, respectively. Initially, the column contains highly saline water (see initial conditions (IC) for aqueous

component concentrations in Table 1).  With the infiltration of fresh water (chemical composition according to Bea et al. 2011) from the left side of the domain (x= 0.0 m), the composition of the pore water in the column changes over time.  The geochemical system includes 10 components and primary species ($Ca^{2+}$, $Na^+$, $Mg^{2+}$, $K^+$, $Cl^-$,  $SO_4^{2-}$, $H^+$, $CO_3^{2-}$, $HS^-$ and $O_2(aq)$), forming 22 secondary species.  The initial composition of pore water and the abundance of minerals and organic matter in the domain, as well as the composition of fresh water (BC), are provided in Table 1.

**Table 1: Initial and Boundary Conditions (IC and BC) for Resident and Infiltrating Fluids, Respectively; Mineral and Organic Matter Abundances for the Verification Example Sulphur**

| Parameter | IC[1] | BC (inflow)[2] | Unit |
|---|---|---|---|
| **Aqueous component concentration** | | | |
| $Ca^{2+}$ | $2.40\times10^{-1}$ | $2.10\times10^{-4}$ | [mol l$^{-1}$] |
| $Na^+$ | 4.09 | $8.22\times10^{-3}$ | [mol l$^{-1}$] |
| $Mg^{2+}$ | $1.40\times10^{-1}$ | $3.99\times10^{-6}$ | [mol l$^{-1}$] |
| $K^+$ | $6.65\times10^{-2}$ | $1.84\times10^{-3}$ | [mol l$^{-1}$] |
| $Cl^-$ | 5.44 | $4.63\times10^{-3}$ | [mol l$^{-1}$] |
| $SO_4^{2-}$ | $6.35\times10^{-3}$ | $1.04\times10^{-15}$ | [mol l$^{-1}$] |
| pH | 5.95 | 7.0 | [-] |
| $CO_3^{2-}$ | $1.27\times10^{-3}$ | $2.73\times10^{-3}$ | [mol l$^{-1}$] |
| $HS^-$ | $3.02\times10^{-15}$ | $3.02\times10^{-15}$ | [mol l$^{-1}$] |
| Eh | -200.00 | 200.00 | [mV] |
| **Mineral volume fraction** | | | |
| **Parameter** | **IC** | | **Unit** |
| $CH_2O$ | 0.10 | | [m$^3$ m$^{-3}$] |
| Calcite | 0.10 | | [m$^3$ m$^{-3}$] |
| Anhydrite | 0.32 | | [m$^3$ m$^{-3}$] |
| Halite | 0.30 | | [m$^3$ m$^{-3}$] |

[1] From Hobbs et al. (2011), Table A-5, Sample ID: SF-3; [2] Bea et al. (2011); mineral volume fractions are assumed data

2.3.3 Parameters

The physical parameters for the homogeneous porous medium are: a porosity of 0.25; a hydraulic conductivity of $1.0\times10^{-3}$ m s$^{-1}$, and a dispersivity of 0.01 m.  The free water diffusion coefficients of all components are set at $1.0\times10^{-9}$ m$^2$ s$^{-1}$.

Based on the observational data from the southern Ontario region of the Michigan Basin, sulphidic waters exist at shallow to intermediate depths (up to around 200 m), while at greater depths the concentration of total sulphide is commonly low (Carter et al. 2015).  It is therefore assumed that biogenic sulphate reduction is almost completely suppressed due to the extremely high salinity (>200 g L$^{-1}$) that is known to exist at greater depths (Hobbs et al. 2011).  In order to simulate this effect, the formulation must be able to simulate the transition from a

high level of activity of the SRB to no activity due to high salinity, while being continually differentiable. Standard hyperbolic inhibition formulations (e.g. Mayer et al., 2001, see also terms for sulphide and oxygen inhibition in equation 2.2 of this report) were evaluated, but were found inadequate to capture the transition from active sulphate reduction to completely inhibited conditions. Alternative formulations can be derived to meet these requirements based on cosine or Gaussian functions, or tabulated values. A cosine function was selected because of its simplicity and ease of implementation. Similar formulations have been previously used in medical science to simulate the inhibition effect of medicine on organ functions (e.g. Pfister et al. 2004). The inhibition term as a function of chloride concentration is here expressed as:

$$k_{sal} = \begin{cases} 1 & , & if\ [Cl^-] < C_L \\ [\cos(a * [Cl^-] + b) + 1]/2 & , & if\ C_L \le [Cl^-] \le C_H \\ 0 & , & if\ [Cl^-] > C_H \end{cases}$$  **Equation 2-4**

where $[Cl^-]$ is the concentration of Cl⁻ [mol L⁻¹]. The coefficients *a* and *b* can be determined based on Cl⁻ concentration levels $C_H$ and $C_L$. $C_L$ is the chloride concentration below which there is no inhibition of sulphate reduction, while above chloride concentration $C_H$, sufate reduction is completely inhibited. The rate of biogenic sulphate reduction between these two concentration values is assumed to follow a cosine function, with the parameters *a* and *b* defined according to Equation 2-5 and Equation 2-6:

$$a = \frac{180}{C_H - C_L}$$  **Equation 2-5**

$$b = -aC_L$$  **Equation 2-6**

The values for $C_H$ and $C_L$ are 1.41 mol L⁻¹ and 0.076 mol L⁻¹, respectively, which are calibrated based on the observational data (Carter et al. 2015). Other reaction rate parameters are: $k_s =$ 1.62×10⁻³ mol L⁻¹ and $k_{sulf}$ = 6.9×10⁻⁹ mol (L bulk)⁻¹s⁻¹ (Gibson et al. 2011). $K_{H_2S}^{in}$ and $K_{O_2}^{in}$ are calibrated in this work to be 3.125×10⁻⁵ mol L⁻¹ and 3.125×10⁻⁹ mol L⁻¹, respectively (also based on the observational data of Carter et al. 2015). The geochemical thermodynamic database is based on the MINTEQ database for MIN3P-THCm with the extension of Pitzer parameters based on the EQ3/6 Yucca Mountain database (Bea et al. 2011). The pitzer.dat database provided with PHREEQC is used in this study for PHREEQC (Parkhurst and Appelo 2013) simulations. For the simulations using both codes, all individual-ion activity coefficients are scaled according to the MacInnes convention (MacInnes 1919).

2.3.4 Results

Simulated results for total concentrations are depicted in Figure 6 and Figure 7. Figure 6 (left) shows the concentration profiles for HS⁻ (solid lines) and SO₄²⁻ (dashed lines) at 1, 5 and 10 hours. Figure 6 (right, solid lines) depicts the corresponding concentration profiles of Cl⁻ at 1, 5 and 10 hours, respectively. The Cl⁻ concentration in the column decreases substantially with the infiltration of fresh water from the left side Figure 6 (right). Due to the dependence of sulphate reduction on Cl⁻, HS⁻ concentrations remain very low where Cl⁻ concentrations are high, even though the concentration of SO₄²⁻ is high as well. Therefore, a peak of elevated HS⁻ concentrations appears in the transition zone with intermediate salinity (Cl-concentrations) and high SO₄²⁻. Peak concentrations of HS⁻ increase with time and move along the flow path.
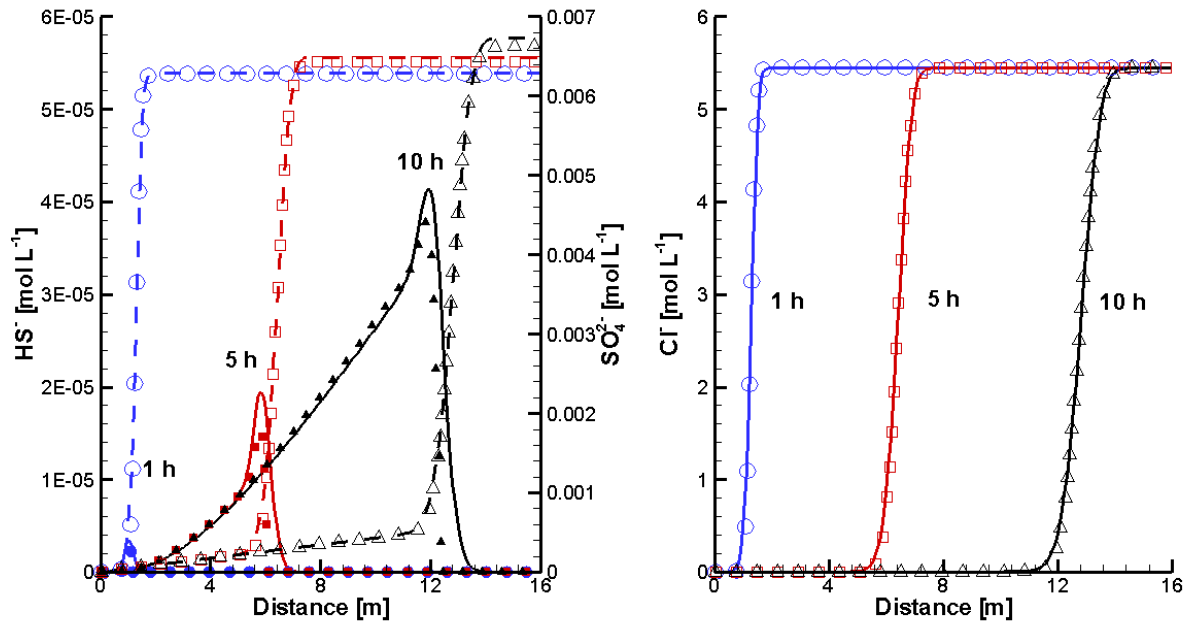
**Figure 6: Comparison of Concentration Profiles of HS⁻ (Solid Lines/Filled Symbols) and SO₄²⁻ (Dashed Lines/Open Symbols) (Left) and Profiles of Cl⁻ (Right) at 1 (Blue), 5 (Red) and 10 (Black) Hours Simulated Using MIN3P-THCm (lines) to Those Simulated Using PHREEQC (Symbols)**

Figure 7 depicts the breakthrough curves of pH, component concentrations and the saturation indices (SI) of minerals.  Calcite is in equilibrium with the pore water (SI = 0.0), while halite is initially slightly undersaturated (SI<0.0).  The initial saturation index of anhydrite is -0.8.  Therefore, anhydrite dissolves and the concentration of $SO_4^{2-}$ increases with time.  Within about 12 hours, the concentrations of the components $Na^+$, $Cl^-$, $Ca^{2+}$, $K^+$ and $Mg^{2+}$ remain almost constant.  The concentration of $SO_4^{2-}$ increases gradually from $6.2\times10^{-3}$ mol $L^{-1}$ to $6.8\times10^{-3}$ mol $L^{-1}$ within 12 hours.  After 12 hours, the fresh water reaches the end of the column and the concentrations of the main components ($Na^+$, $Cl^-$, $Ca^{2+}$, $K^+$, $Mg^{2+}$ and $SO_4^{2-}$) approach constant levels.  The concentration of $HS^-$ at the end of the column remains initially low due to elevated $Cl^-$ concentrations, but substantially increases after 12 hours indicating the arrival of the migration front of the fresh water.  The concentration of $HS^-$ increases thereafter and reaches a plateau at $5.0\times10^{-5}$ mol $L^{-1}$ at about 13 hours.

Comparison of the simulated results obtained by MIN3P-THCm (lines in Figure 6 and Figure 7) with those obtained by PHREEQC (symbols in Figure 6 and Figure 7) shows very good agreement.  Figure 6 (left) shows a small difference in the concentration profiles for $HS^-$, which may be due to the different spatial and temporal weighting schemes employed by the two codes or differences in the thermodynamic databases. The good agreement builds confidence in the correct implementation of the SDSR model in MIN3P-THCm in comparison with PHREEQC.
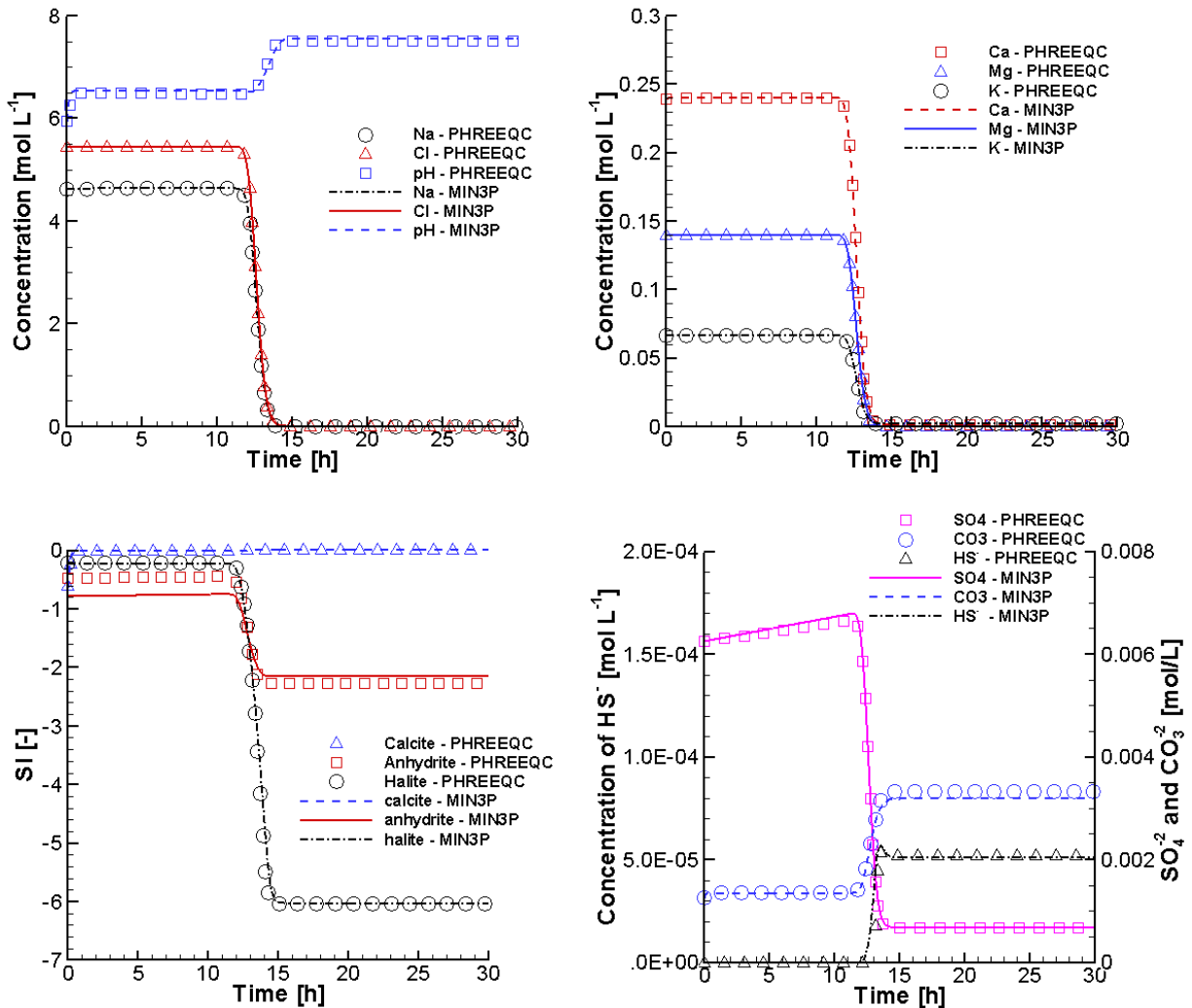
**Figure 7: Comparison of Breakthrough Curves of pH and Total Concentrations of Na⁺ and Cl⁻ (Top Left), Mg²⁺, Ca²⁺, K⁺ (Top Right), SO₄²⁻, CO₃²⁻ and HS⁻ (Bottom Right), and SI (saturation indexes) of Calcite, Anhydrite and Halite (Bottom Left) Simulated by MIN3P-THCm (Lines) to Those Calculated by PHREEQC (Symbols) – With Inhibition of Sulphate Reduction by Cl⁻**

To demonstrate the influence of the SDSR inhibition term on the results, comparison simulations were performed for the same example, but without the SDSR inhibition term. Figure 8 depicts the simulated breakthrough curves for pH and total component concentrations, together with the SI curves of the minerals.  In comparison to the breakthrough curves obtained with the SDSR inhibition term, most components with the exception of HS⁻ and $CO_3^{2-}$ show no significant differences (compare Figure 7 and Figure 8).  However, as expected, substantial differences exist for the total concentrations of HS⁻. If the influence of salinity on sulphate reduction is not taken into account, HS⁻ forms from the beginning of the simulation and increases rapidly within 12 hours, reaching peak concentrations of 1.4×10⁻⁴ mol L⁻¹ at about 12 hours.
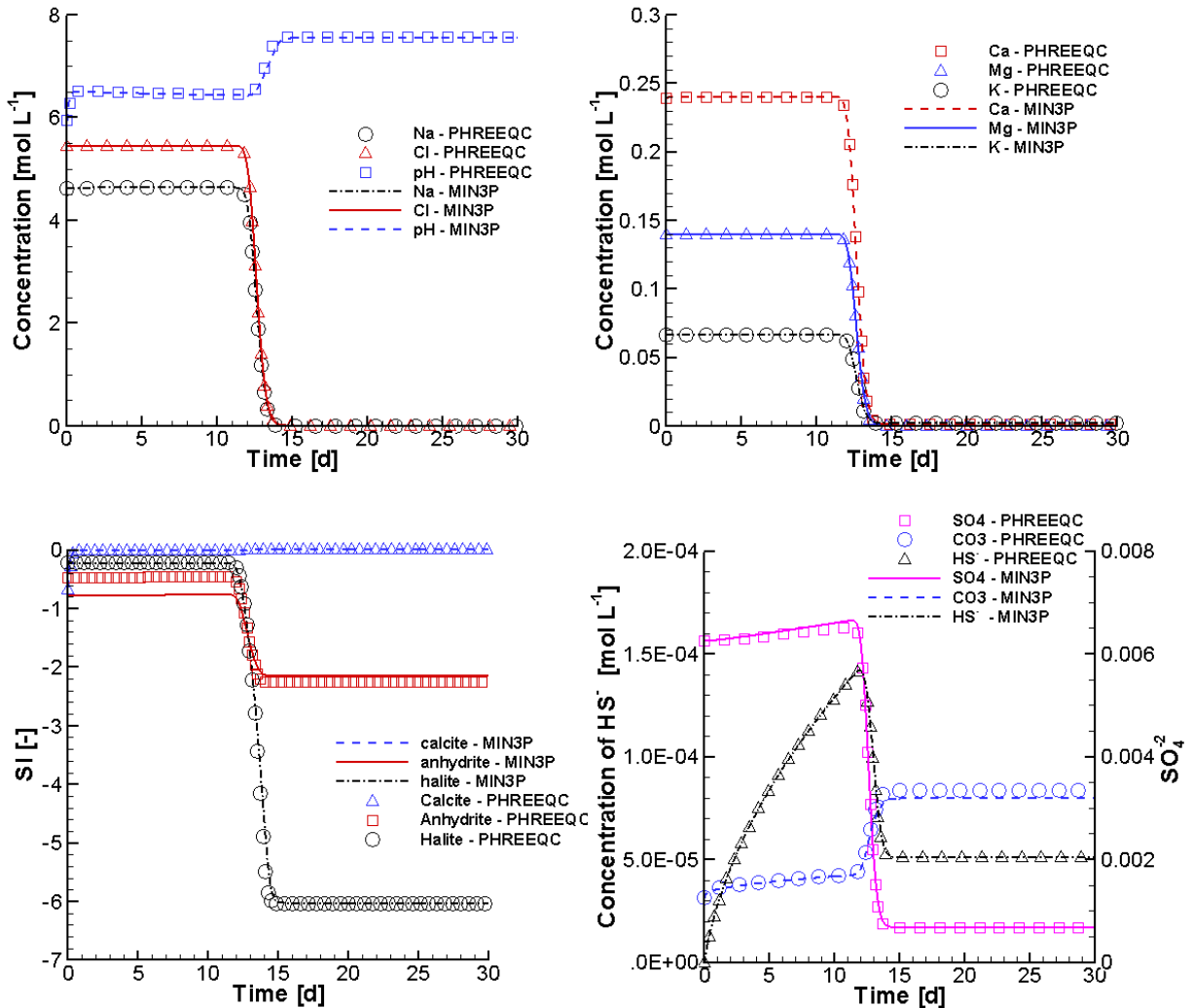
**Figure 8: Comparison of Breakthrough Curves of pH and Total Concentrations of Na$^+$ and Cl$^-$ (Top Left), Ca$^{2+}$, K$^+$, Mg$^{2+}$ (Top Right), SO$_4^{2-}$, CO$_3^{2-}$ and HS$^-$ (Bottom Right), and SI (saturation indexes) of Calcite, Anhydrite and Halite (Bottom Left) Simulated by MIN3P-THCm (Lines) to Those Calculated by PHREEQC (Symbols) – Without Inhibition of Sulphate Reduction by Cl$^-$**

## 3.   NUMERICAL INVESTIGATION OF THE FORMATION OF SULPHIDIC WATERS IN A SEDIMENTARY BASIN

The SDSR model is applied to investigate controls on the formation of sulphidic waters in a generic 2D sedimentary basin as described by Bea et al. (2011) and Bea et al. (2016).  Most parameters used to define the model geometry and discretization, rock type distribution, hydraulic properties (including the depth-dependent porosity, hydraulic conductivities, and specific storage), mechanical properties, thermal properties, dispersivities, and the glaciation

and deglaciation scenarios, are the same as used for the illustrative example presented in Bea et al. (2016).  Detailed descriptions of the parameter selection and their dependence on the rock type, and on depth, can be found in Bea et al. (2011, 2016).  The main difference in the current simulations is the modification of the geochemical system through the addition of a new component (HS$^-$) and the related secondary species (i.e. $H_2S$(aq) and $S^{2-}$) to facilitate simulation of biogenic sulphate reduction.  In addition, the oxidation of an organic substance by dissolved oxygen is considered in the case of the OXYGEN-COMSUMPTION simulation (see section 3.3).

Although relatively complex, the current conceptual model of sulphate reduction is simplified in comparison to field conditions.  For instance, hydrogen sulphide may also partition into resident gas pockets present in the formations, or react with metals, in particular ferrous iron, and precipitate to form sparingly soluble mineral phases.  It is also possible that re-oxidation of sulphide to sulphur or sulphate may occur, in particular under the dynamic conditions of a glaciation/deglaciation scenario.  In addition, uneven spatial recharge together with seasonal precipitation patterns can lead to local groundwater circulation and discharge into surface water bodies, providing an additional sink for dissolved sulphide present in shallow and intermediate-depth groundwater.  Furthermore, the temperature-dependence of sulphate reduction was not included in the current simulations.  Consideration of these processes was beyond the scope of the current study.

## 3.1  CONCEPTUAL MODEL AND PHYSICAL PARAMETERS

The physical domain used for the simulations is a symmetrical two-dimensional generic model that includes the key features of several sedimentary basins located in eastern North America, identical to the domain presented in Bea et al. (2011, 2016).  The model includes 14 rock types (Figure 9) with different porosity and hydraulic conductivities that decrease with depth (Figure 10 and Figure 11).  The domain (Figure 9) was discretized into 45,000 control volumes.
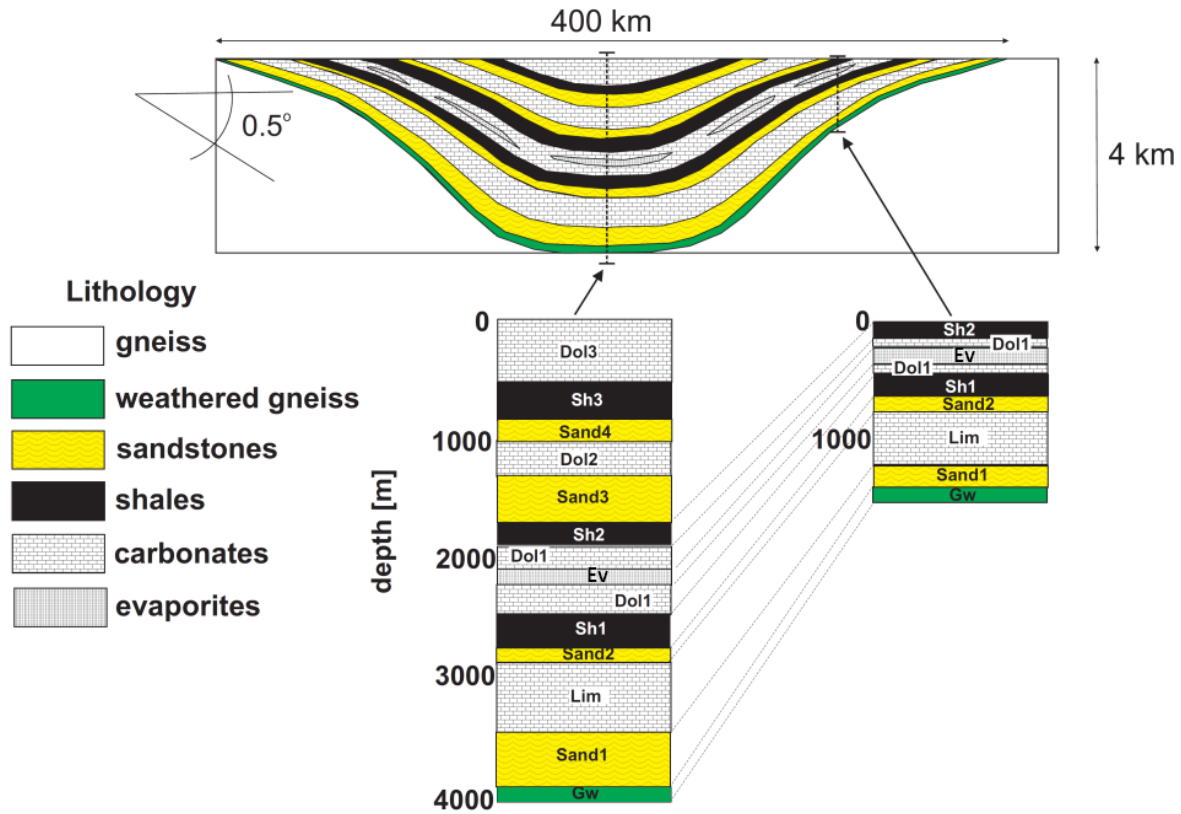
**Figure 9: Geometry and Main Hydrogeological Units Considered (Bea et al. 2011)**

The porosities of the rocks generally decrease with depth in sedimentary basins (e.g. as observed in Mount Simon sandstones in the Illinois Basin by Medina et al. (2011) and Bea et al. (2011)). The depth-dependent initial porosity ($\phi(z)$, [-]) is shown in Figure 10.



porosity: 0.01 0.02 0.03 0.04 0.05 0.06 0.07 0.08 0.09 0.1 0.11 0.12 0.13 0.14 0.15 0.16
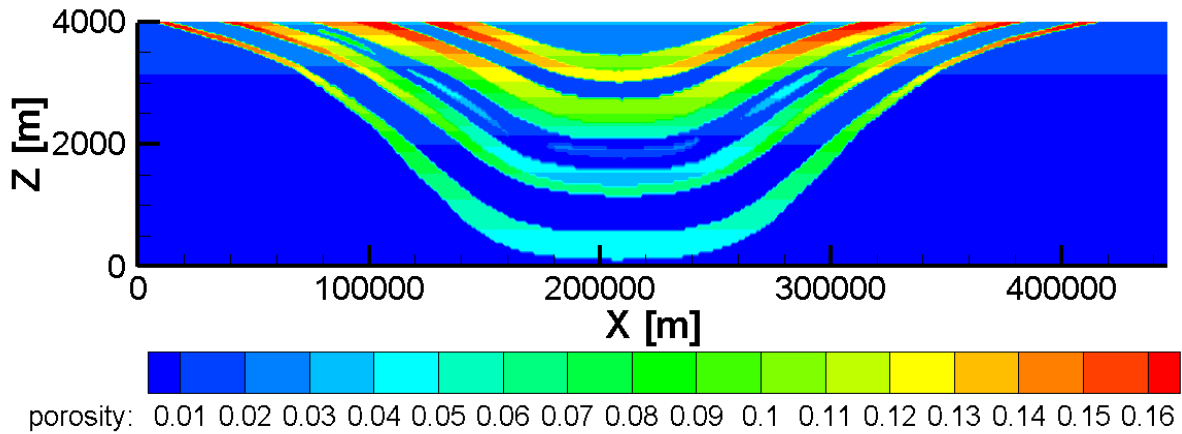
**Figure 10: Distribution of Initial Porosity (According to Bea et al. 2011)**

The hydraulic conductivity tensor (Figure 11) is also assumed to vary with depth. Its dependence on depth is captured by defining the permeability tensor **k**(z) as a function of the porosity field and is calculated based on the Carman-Kozeny expression (Bea et al. 2011).
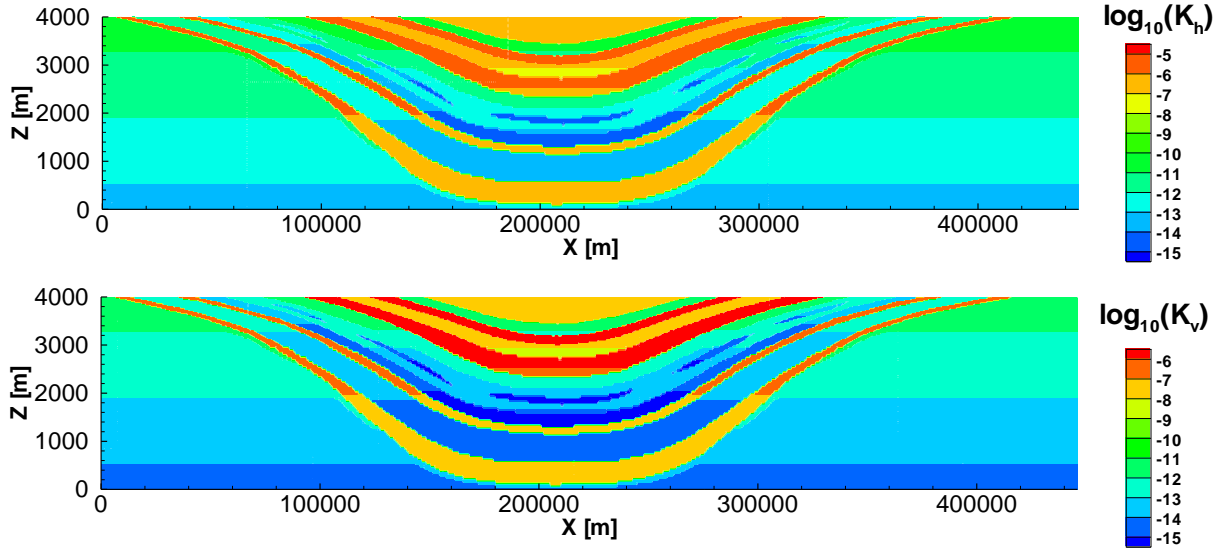


**Figure 11: Profiles of Initial Horizontal (Upper Panel) and Vertical (Lower Panel) Hydraulic Conductivities (in log$_{10}$[m s$^{-1}$])**

A free water diffusion coefficient of $10^{-9}$ m$^2$ s$^{-1}$ was assumed for all dissolved species. Effective diffusion coefficients were calculated as a function of porosity and tortuosity according to the Millington formulation (see Mayer et al. 2002). This implies that the effective diffusion coefficients vary with porosity, depending on the hydrogeological units, and decrease with depth. The main hydrogeologic parameters used for the simulations are summarized in Table 2.

Additional parameters for the simulations are related to the salinity dependent sulphate reduction model using a simplified Monod-type rate expression as described in Equation 2-2 and Equation 2-3 in section 2.1 and Equation 2-4 in section 2.3.3.

The reaction parameters are the same as used in the verification example described in section 2.3.3. The oxidation of organic substances by dissolved oxygen, which was not considered in the verification example, is described in Equation 3-1:

$$CH_2O + O_2(aq) \rightarrow CO_3^{2-} + 2\,H^+$$

**Equation 3-1**

This reaction is simulated as an irreversible dissolution reaction using a simplified Monod-type rate expression of the form:

$$R = -k_{org}\left[\frac{[O_2(aq)]}{k_{s1} + [O_2(aq)]}\right]$$

**Equation 3-2**

in which $k_{org}$ is the rate constant, set to 1.0×10⁻⁹ mol (L bulk)⁻¹ s⁻¹ (Middelburg 1989), and $k_{s1}$ is the half-saturation constant for $O_2(aq)$, which was calibrated to be 3.125×10⁻⁶ mol L⁻¹.

The geochemical thermodynamic database is the same as described in section 2.3.3.

**Table 2: Hydrogeologic Parameters Used in the Simulations. Values Given are for a Location Corresponding to the Center of the Sedimentary Basin (Bea et al. 2011)**

| Unit | Lithology | Depth [m] | $\phi$ [-] | $Log_{10} K_H$ [m s⁻¹] | $Log_{10} K_v$ [m s⁻¹] | $S_S{}^*$ [m⁻¹] |
|---|---|---|---|---|---|---|
| Dol3 | Dolostone | 200 | 0.027 | -6.3 | -7.3 | 3.1 x 10⁻⁷ |
| Sh3 | Shale | 700 | 0.102 | -11.0 | -12.0 | 1.1 x 10⁻⁶ |
| Sand4 | Sandstone | 900 | 0.124 | -5.7 | -5.7 | 9.2 x 10⁻⁷ |
| Dol2 | Dolostone | 1100 | 0.016 | -7.0 | -8.0 | 2.6 x 10⁻⁷ |
| Sand3 | Sandstone | 1500 | 0.100 | -6.0 | -6.0 | 8.1 x 10⁻⁷ |
| Sh2 | Shale | 1800 | 0.057 | -11.8 | -12.8 | 8.9 x 10⁻⁷ |
| Dol1 | Dolostone | 2000 | 0.009 | -12.7 | -13.7 | 2.3 x 10⁻⁷ |
| Ev | Evaporites | 2150 | 0.019 | -14.9 | -15.9 | 4.5 x 10⁻⁷ |
| Sh1 | Shale | 2500 | 0.039 | -14.4 | -15.4 | 8.1 x 10⁻⁷ |
| Sand2 | Sandstone | 2800 | 0.063 | -6.4 | -7.4 | 6.5 x 10⁻⁷ |
| Lim | Limestone | 3200 | 0.005 | -13.7 | -14.7 | 1.9 x 10⁻⁷ |
| Sand1 | Sandstone | 3700 | 0.045 | -6.8 | -7.8 | 5.7 x 10⁻⁷ |
| Gw | Weathered Gneiss | 3950 | 0.002 | -12.9 | -13.9 | 5.4 x 10⁻⁷ |
| #G | Gneiss | 4000 | 0.002 | -13.4 | -14.5 | 1.6 x 10⁻⁷ |

$S_S{}^*$ – specific storage. #G – The Gneiss exists below the Gw-unit as shown in Figure 9.

## 3.2   SIMULATION CASES

The key parameters controlling sulphide production according to Equation 2-1 to Equation 2-3 are sulphate, oxygen and sulphide concentrations, as well as salinity (represented by Cl$^-$).  To investigate the influence of these factors on the formation and distribution of hydrogen sulphide, three cases were considered: the case BASE, the case ELEVATED-SULPHATE (with higher sulphate concentrations near the top boundary), and the case OXYGEN-CONSUMPTION (same as the case BASE, but including a kinetic reaction to simulate the consumption of oxygen by organic carbon).  For each case, two scenarios were considered: 1) an inter-glacial scenario – with constant flow boundary conditions along the top of the domain; and 2) a transient glaciation – deglaciation scenario.  The initial and boundary conditions for flow and heat transport for all the cases and scenarios are the same, and are consistent with previous work by Bea et al. (2011, 2016).  The initial conditions for each simulation type are described in subsection 3.3.

The flow boundary conditions for the inter-glacial scenario are: in the center of the top boundary (i.e. x=200 km), the pressure head is 4100 m.  From the center, the pressure head linearly decreases to 4000 m towards both sides, identical to the boundary condition illustrated in Figure 13 for Stage IV.  This flow boundary condition results in a small horizontal hydraulic gradient along the top boundary (i.e. $5.0\times10^{-4}$ from x=0 to 200 km, and $4.2\times10^{-4}$ for the remaining part of the top boundary).  No-flow boundaries are applied to the bottom and on both sides of the domain.

For the glaciation-deglaciation scenario, the boundary conditions along the top boundary change because of ice sheet dynamics (Figure 13).  A single glaciation-deglaciation cycle is assumed with cold-based conditions (i.e. no meltwater) during the ice sheet advance, followed by a stable glacial maximum and continuing cold-based conditions, and by a subsequent warm-based (i.e. meltwater production) ice sheet retreat.  The scenario is subdivided into four stages following the approach presented by Bense and Person (2008) and by Bea et al. (2011, 2016).  The scenario is depicted in Figure 12 and consists of:

- Stage I, linear ice sheet accumulation, i.e. ice sheet advance (from 0 to 12500 years) from the right towards left;
- Stage II, constant ice sheet thickness with a thickness of 2000 m (lasting for 5000 years);
- Stage III, melting, i.e. ice sheet retreat (lasting for 5000 years); and
- Stage IV, no ice sheet present, interglacial conditions

The maximum ice sheet thickness and extent used in the current study are 2 km and 440 km, respectively, implying complete ice coverage of the basin during the Stage II glacial maximum.
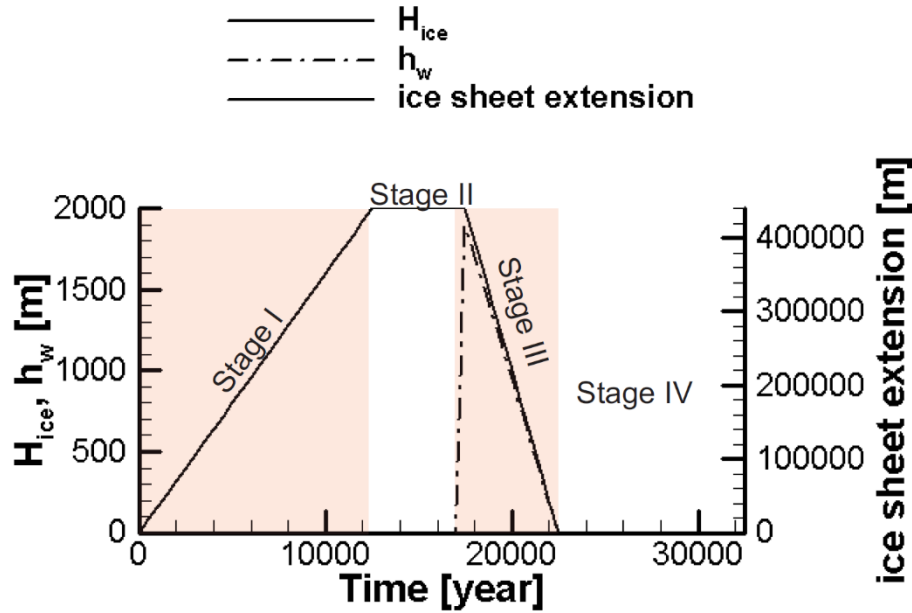
**Figure 12: Glaciation Scenario Used to Specify Boundary Conditions at the Surface of the Sedimentary Basin Domain, where: $H_{ice}$ is the Ice Sheet Thickness at the Right-hand Edge of the Domain; $h_w$ is the Hydraulic Head Applied Beneath the Ice Sheet During Stage III; the Ice Sheet Extension is Measured from the Right-hand Edge (Bea et al. 2011)**

The boundary conditions (BCs) at different stages are changing during the course of ice sheet advancement/retreat as schematically depicted in Figure 13.  During stage I, the ice advances from the right hand side.  A no-flow boundary is applied to the ice-covered part of the top boundary.  Due to hydro-mechanical coupling effects, the load of the ice increases the hydraulic pressure of the pore water present in formations underneath the ice sheet, which is valid for all cases with an ice sheet present on the top boundary of the domain (Bea et al. 2011).  The remaining part of the top boundary retains the same boundary condition for flow as for the aforementioned inter-glaciation scenarios.  During stage II, the top boundary is fully covered by the ice sheet and a no-flow boundary is applied across the entire basin.  When the ice starts to retreat from the left hand side during the Stage III, melt water within the ice sheet is assumed to exert a hydraulic head on the ground surface at a value equal to the thickness of the ice sheet times 0.95 (Bea et al. 2011).  At the beginning, the maximum hydraulic head is 1900 m, defined as a fraction of 0.95 of the maximum ice sheet thickness of 2000 m in-line with previous work (Bense and Person 2008, Bea et al. 2011).  Locally, the hydraulic head at the ice/rock interface depends on the position relative to the retreating front and tends to decrease as the ice sheet continues to retreat.  In this case, the lateral and vertical hydraulic gradients are much higher than those applied for the inter-glacial scenario. During the period of deglaciation, it is assumed that the left part of the top boundary without ice coverage reassumes the same flow boundary condition as for the inter-glacial scenario.  After the ice sheet has completely retreated (i.e. Stage IV), the flow boundary condition is the same as for the inter-glacial scenario (Figure 13).
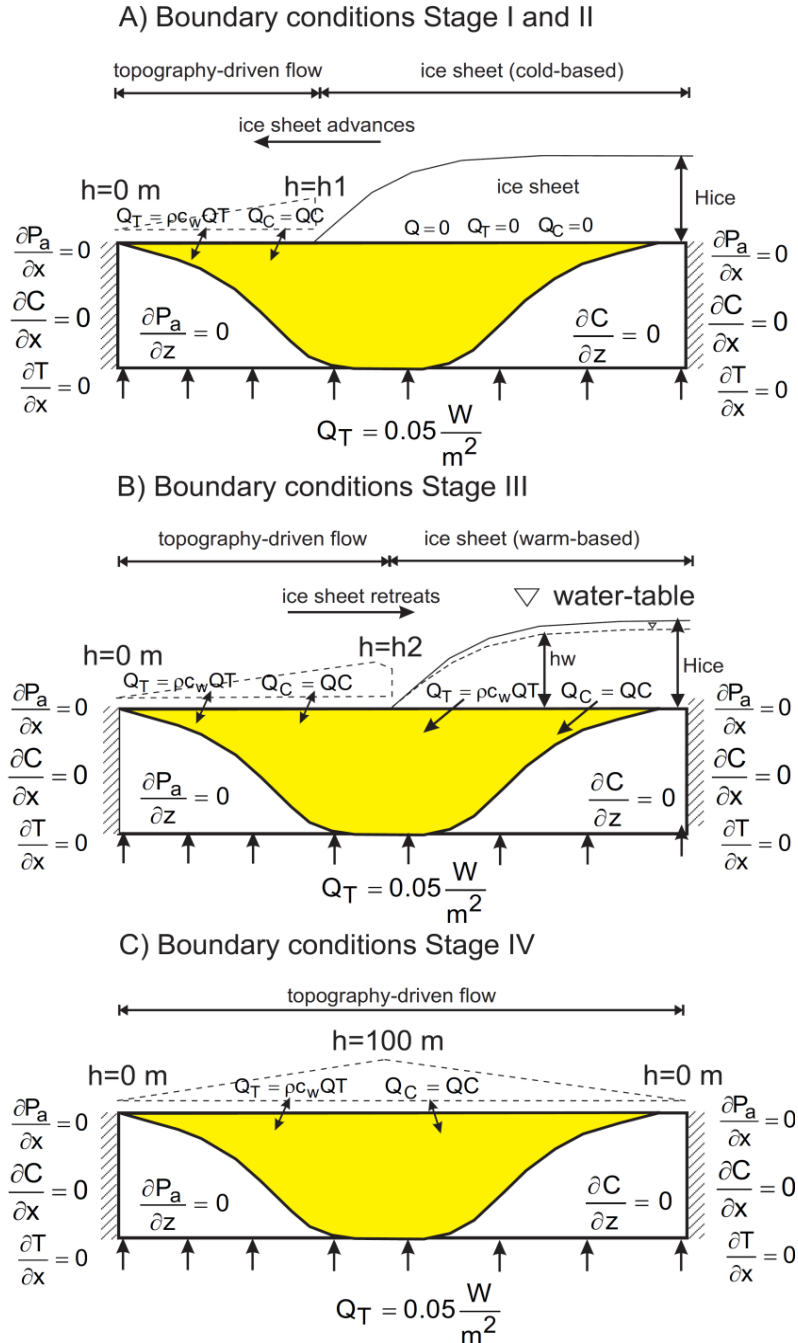
**Figure 13: Boundary Conditions Imposed in the Simulations: A) Stage I (i.e. Ice Sheet Accumulation) and Stage II (i.e. Constant Ice Sheet Thickness). B) Stage III (i.e. Ice Sheet Retreat). C) No Ice Present (i.e. Present Day Conditions). Q is the Volumetric Recharge or Discharge per Unit Area, $Q_c$ is the Solute Mass Flux per Unit Area, C is Solute Concentration, h is the Hydraulic Head in Ice-Free Areas, $H_{ice}$ is the Maximum Ice Sheet Thickness, and $h_w$ is the Hydraulic Head beneath the Ice Sheet. $Q_T$ is the Energy Flux per Unit Area, T is the Water Temperature, and $c_w$ is the Specific Heat Capacity of Water (Bea et al. 2011)**

## 3.3 GEOCHEMICAL PARAMETERS AND INITIAL CONDITIONS

The geochemical system included in the simulations considered 10 components ($Ca^{2+}$, $Na^+$, $Mg^{2+}$, $K^+$, $Cl^-$, $SO_4^{2-}$, $H^+$, $CO_3^{2-}$, $HS^-$ and $O_2(aq)$) and 22 secondary aqueous species. It was assumed that organic substances are available in most basin rocks except in the gneiss, weathered gneiss and the evaporite deposits. Dissolution of anhydrite present in the evaporites is the main source of sulphate. Additional geochemical reactions include calcite and dolomite dissolution/precipitation, providing pH-buffering, as well as anhydrite which provides important controls on the solubility of $SO_4^{2-}$ and $H_2S$. Thermodynamic constants for the homogeneous and heterogeneous reactions were taken from the EQ3/6 database by Wolery and Jarek (2003). The selectivity coefficients for ion exchange reactions were taken from Appelo and Postma (2005). The virial coefficients for the Pitzer model were based on the HMW model (Harvie et al. 1984; at 25 °C and 1 atm). Reactions considered in the geochemical system are listed in Table 3 of Bea et al. (2011). For the simulations considered here, the biogenic reduction of sulphate was also included (Equation 2-1 in section 2.1).

Homogeneous intra-aqueous reactions are assumed to be in equilibrium. On the time scales of interest, the concentrations of most aqueous components in shallow crustal waters are controlled by mineral solubilities. Thus, most mineral dissolution-precipitation reactions are considered to be thermodynamically-controlled. Equilibrium mineral phases included halite (NaCl), calcite ($CaCO_3$), and anhydrite ($CaSO_4$). Anhydrite was chosen as the Ca-$SO_4$ mineral phase because it is reported to be geochemically significant in several sedimentary basins (e.g. the Michigan and Appalachian basins (McIntosh and Walter 2005); gypsum was not included in the current simulations because the simultaneous presence of both anhydrite and gypsum would cause a Gibbs' phase rule violation.

In sedimentary basins, fresh to brackish waters are predominant in shallow groundwater flow systems. However, more concentrated fluids, including saline waters and brines, are present at greater depths (e.g. Hanor 1987; McIntosh and Walter 2005; Hobbs et al. 2011). The chemical compositions of the brines considered in the present study were initially based on data compiled by Hobbs et al. (2011) and Carter et al. (2015). When defining initial conditions for the model the chemical compositions of the brines were modified to be in equilibrium with the mineral phases present in the corresponding sedimentary units.

The chemical composition of recharge water for all simulations was representative of meteoric water. The composition of meteoric water shown in Table 3 was taken from Bea et al. (2004, 2011) and was equilibrated with present-day atmospheric $CO_2(g)$ (about $3.4 \times 10^{-4}$ atm).

Based on observational data (INTERA 2011; Carter et al. 2015), solute concentrations of the main components increase with depth. To represent this increase in the simulations, the concentrations of the main components were assumed to linearly increase from the top boundary (the concentration of the components (5) in Table 3) to the formation water composition at a depth of 300 meters (Table 3). The initial total component concentration profiles are depicted in Figure 14.

**Table 3: Chemical Composition of Brines in Deep Groundwater and Meteoric Water Used for Case BASE**

| | Formation and boundary water compositions | | | | |
|---|---|---|---|---|---|
| | **(1)** | **(2)** | **(3)** | **(4)** | **(5)** |
| pH | 6.0 | 6.0 | 6.0 | 6.0 | 6.0 |
| $Ca^{2+}$ [mol $l^{-1}$] | 1.50 | 0.77 | 0.20 | 0.19 | $6.2 \times 10^{-4}$ |
| $Mg^{2+}$ [mol $l^{-1}$] | $6.5 \times 10^{-2}$ | $4 \times 10^{-2}$ | $8.6 \times 10^{-3}$ | $10^{-2}$ | $8.2 \times 10^{-4}$ |
| $Cl^-$ [mol $l^{-1}$] | 6.22 | 4.16 | 6.23 | 3.92 | $2.9 \times 10^{-3}$ |
| $SO_4^{2-}$ [mol $l^{-1}$] | $5.4 \times 10^{-4}$ | $4 \times 10^{-3}$ | $2.1 \times 10^{-2}$ | $5.2 \times 10^{-5}$ | $2.6 \times 10^{-4}$ |
| $K^+$ [mol $l^{-1}$] | $3.4 \times 10^{-2}$ | $5.7 \times 10^{-2}$ | 0.07 | 0.12 | $6.4 \times 10^{-5}$ |
| TIC* [mol $l^{-1}$] | $1.2 \times 10^{-4}$ | $3.2 \times 10^{-4}$ | $5.2 \times 10^{-4}$ | $1.8 \times 10^{-3}$ | $1.7 \times 10^{-5}$ |
| $Na^+$ [mol $l^{-1}$] | 2.85 | 2.49 | 5.77 | 3.00 | $5.2 \times 10^{-4}$ |
| $HS^-$ [mol $l^{-1}$] | $6.0 \times 10^{-6}$ | $3.5 \times 10^{-5}$ | $4.0 \times 10^{-5}$ | $4.0 \times 10^{-6}$ | $1.0 \times 10^{-8}$ |
| $O_2(aq)$ [mol $l^{-1}$] | $1.0 \times 10^{-20}$ | $1.0 \times 10^{-20}$ | $1.0 \times 10^{-20}$ | $1.0 \times 10^{-20}$ | $2.6 \times 10^{-4}$ |
| Chemical signature | Ca-Na-Cl | Na-Cl | Na-Cl | Na-Cl | Ca-Mg-Cl |
| Salinity [g $l^{-1}$] | 353 | 239 | 366 | 230 | $2.0 \times 10^{-4}$ |
| Density [kg $m^{-3}$] | 1211 | 1150 | 1204 | 1128 | 997 |

(1) Units G, Gw, Sand1 and Sand2.
(2) Units Lim, Sh1 and Dol1.
(3) Unit Ev.
(4) Units Sh2, Sand3, Sand4, Sh3, Dol2 and Dol3.
(5) Meteoric water.
* Total Inorganic Carbon
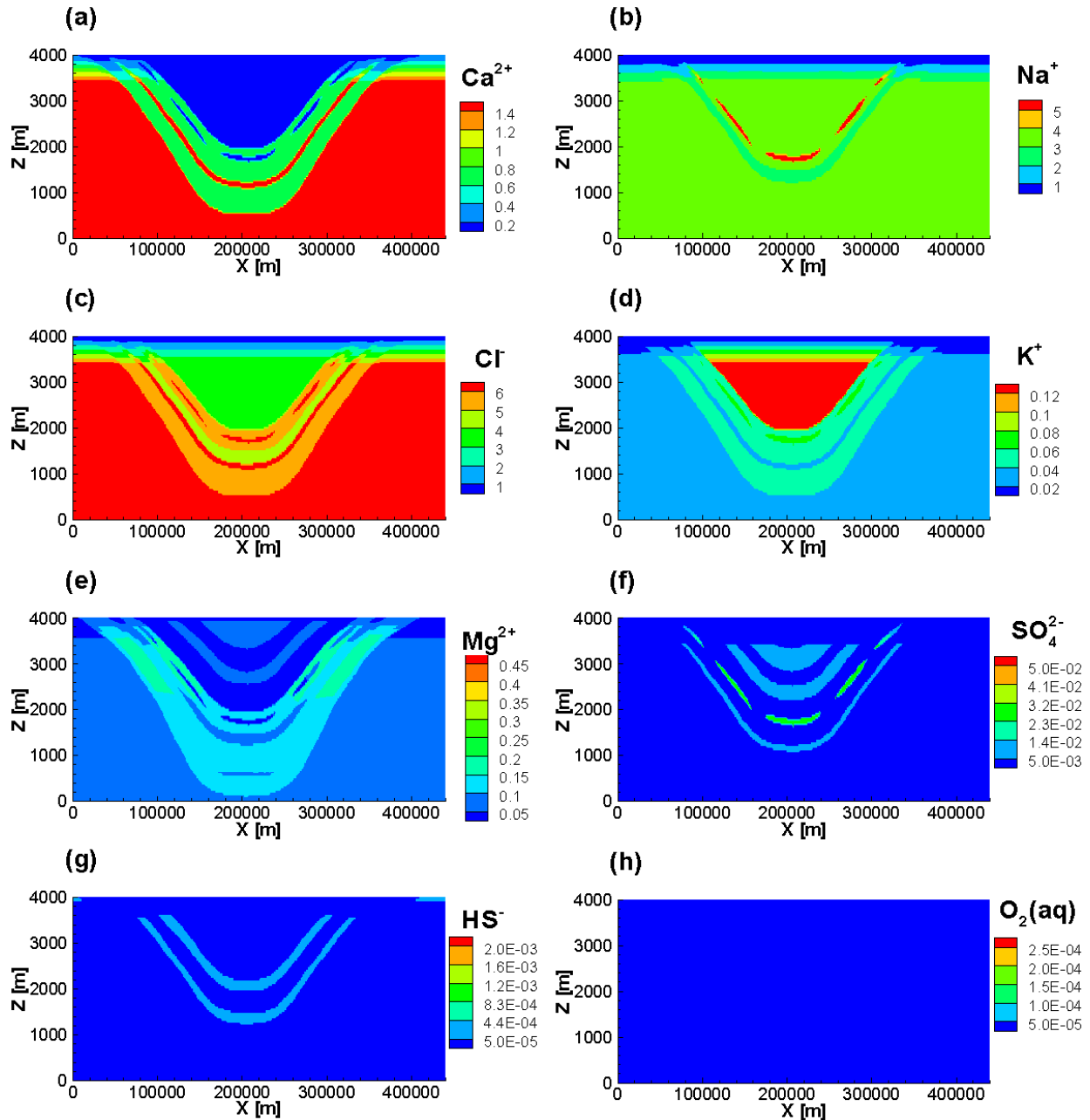
**Figure 14: Initial Total Concentrations of Chemical Components for the Case BASE (in [mol L$^{-1}$])**

The simulation for the case ELEVATED-SULPHATE uses the same initial conditions as the case BASE for all components except SO$_4^{2-}$ as depicted in Figure 15, i.e. with higher sulphate concentrations present in groundwater near the top boundary. This adjustment was made to investigate the effect of SO$_4^{2-}$ concentrations on the formation of sulphidic waters in the subsurface. The concentrations of SO$_4^{2-}$ near the right margin of the basin were set within the range of observed data (Carter et al. 2015) to represent conditions in Southern Ontario, located on the flank of the Michigan Basin (Figure 3). So far, no geochemical data from the central

region of the Michigan Basin are available. $SO_4^{2-}$ concentrations in the central upper region remained the same as case BASE.
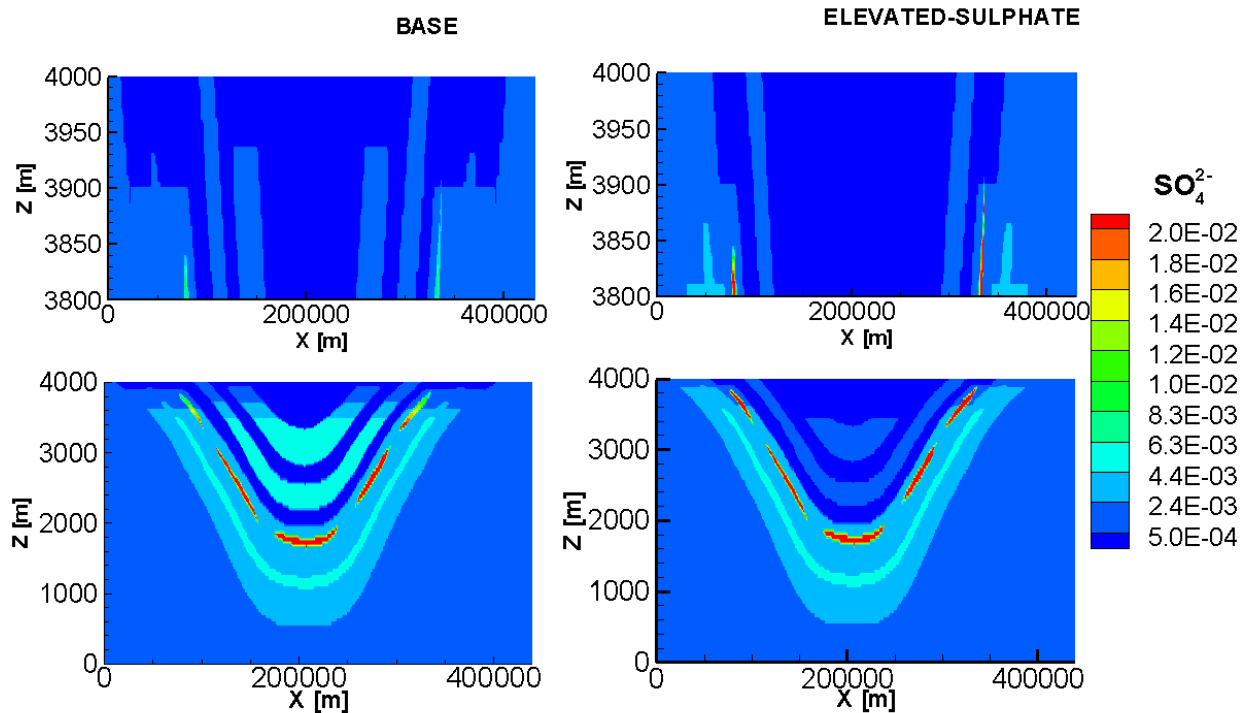


**Figure 15: Comparison of the Initial $SO_4^{2-}$ Concentration (in [mol $L^{-1}$]) for the Case BASE (left) and the Case ELEVATED-SULPHATE (right)**

For the case OXYGEN-CONSUMPTION, the consumption of dissolved oxygen by organic matter was considered. Oxygen consumption by organic matter only occurs near the top boundary because no oxygen is available in deeper horizons.

## 3.4    SIMULATION RESULTS – INTER-GLACIATION

### 3.4.1 Case BASE

At quasi-steady state (at $3.25 \times 10^4$ years), the distribution of component concentrations is controlled by the geochemical reactions, the initial conditions, and the boundary conditions (Figure 16). Ingress of meteoric water across the top boundary explains the presence of dilute groundwater near the top boundary. Highly concentrated formation waters have much higher fluid density than the meteoric water, which limits the downward movement of the meteoric water. Simulated results show that the zone affected by the ingress of meteoric water from the top boundary is generally limited to a depth of around 200 m below the ground surface (Figure 16). The concentration of $Cl^-$ remains high in the deeper subsurface, inhibiting biogenic sulphate reduction (Figure 16(c)). Dissolved oxygen in the meteoric water penetrates deeper in the central region owing to elevated hydraulic heads in this region. The maximal depth of

oxygen penetration is about 100 m, even though oxygen is assumed to behave conservatively in this simulation.

Sulphate is released by the dissolution of anhydrite, which exists mainly in the lenses of evaporites imbedded in the layer dolostone-1. Consequently, the sulphate concentration in this region, and the region adjacent to the evaporites, is the highest. Small amounts of anhydrite in the shales and sandstones are also a source of sulphate. The most favorable geochemical conditions for sulphate reduction are: low salinity (i.e. $Cl^-$), elevated sulphate concentrations, low sulphide concentrations, and low oxygen concentrations. Simulated results show that suitable conditions for sulphate reduction are present to a depth of approximately 200 m, being most favorable around 150 m (Figure 16). Sulphate concentrations in the most favorable zone decrease over the $3.25\times10^4$ year simulation period.
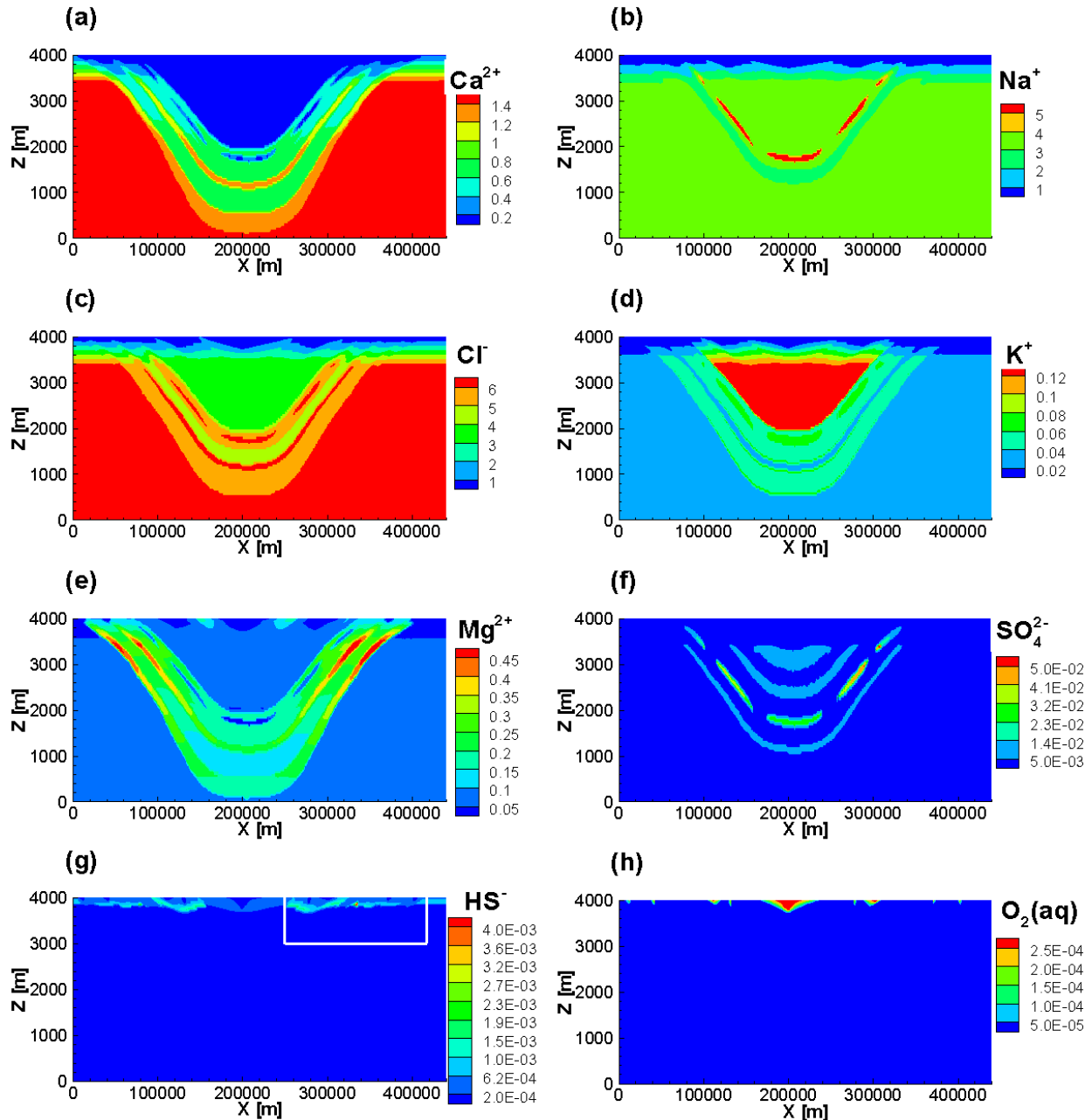
**Figure 16: Total Concentration Contours (in [mol L$^{-1}$]) of Chemical Components for the case BASE at 3.25×10$^4$ Years. White Rectangle Indicates the Data Extraction Region (i.e. Horizontal Extent from 250 to 420 km and Vertical Extent from 3000 to 4000 m) for HS$^-$ Concentrations Shown in Figure 17**

To qualitatively compare the observed sulphide data (Carter et al. 2015) with results from the 2D generic simulations, the total HS$^-$ concentrations within a rectangular zone near the right flank of the basin (indicated by the white rectangle in Figure 16(g)) were extracted from the simulation results. The extracted area covers a region of similar size to that of the Michigan Basin within southern Ontario (Figure 2). The simulated data values were obtained for 100 vertical profiles, each with 30 points. Average and standard deviations were calculated from

the 100 vertical profiles at each depth interval and these are depicted in Figure 17. Considering that the observed data are from numerous separate wells over a large spatial extent in southern Ontario (Figure 1 and Figure 2), and the simulation results are for a generic sedimentary basin model, the simulated vertical profiles of HS$^-$ generally agree with the observed concentrations. The larger range in observed HS$^-$ concentration (especially the very low concentrations) between 4,000 m and 3,800 m might be due to the fact that the simulations did not consider oxidation of hydrogen sulphide, or reactions with metals (e.g. ferrous iron) leading to the formation of sparsely soluble sulphide minerals.  In addition, uneven spatial recharge together with seasonal precipitation patterns can lead to local groundwater circulation and discharge into surface water bodies, providing an additional sink for dissolved sulphide present in shallow and intermediate-depth groundwater.
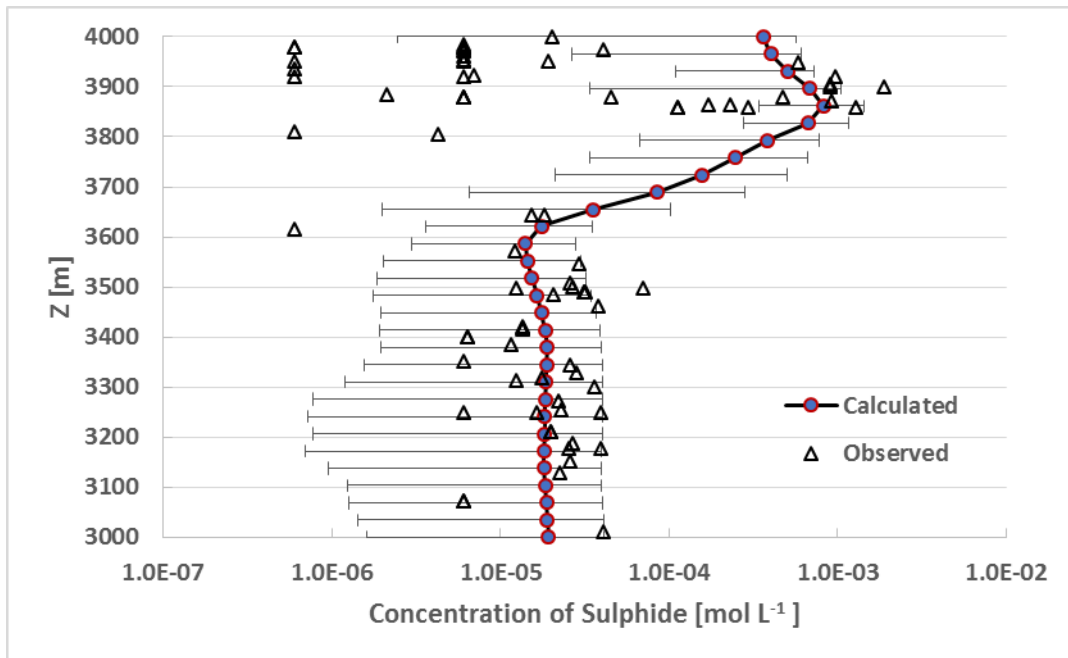


**Figure 17: Comparison of the Observed Sulphide Data and the Simulated Average HS$^-$ Concentrations (in [mol L$^{-1}$]) +/- Standard Deviations (Horizontal Black Lines) at Different Depths for the Region Shown in Figure 16(g).  Simulation Results are for 3.25×10$^4$ Years under Interglacial Conditions; Observed Data are from Carter et al. (2015)**

3.4.2 Case ELEVATED-SULPHATE

Simulation results for the case ELEVATED-SULPHATE (Figure 18) show a similar distribution for HS$^-$ as the case BASE.  In comparison to the case BASE, more sulphate is present in the top 150 m of the domain, which consequently results in higher average HS$^-$ concentrations in this depth interval with the maximum value being 1.69×10$^{-3}$ mol L$^{-1}$ (Figure 19), much higher than that for the case BASE with 6.69×10$^{-4}$ mol L$^{-1}$ (Figure 17).
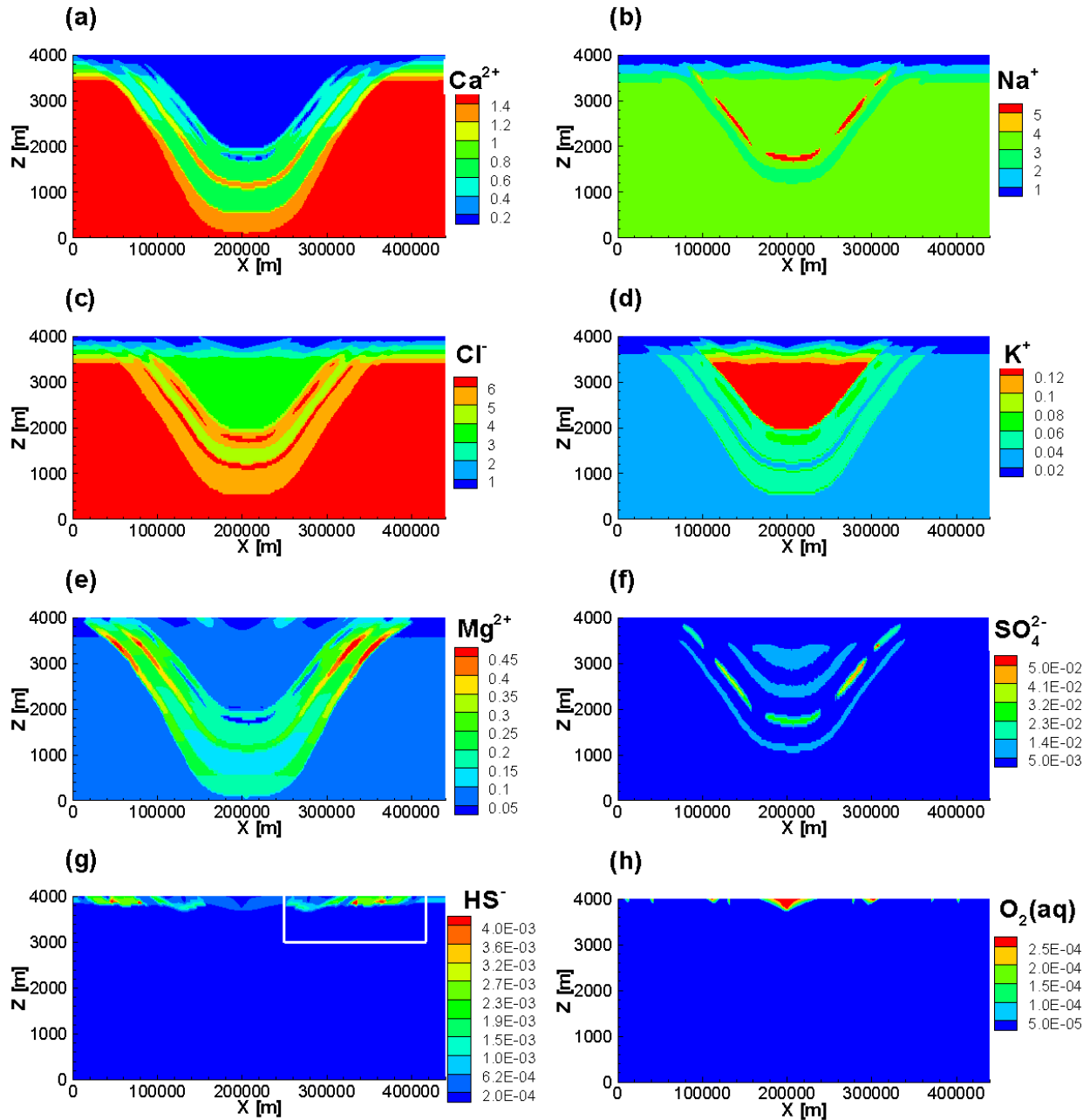
**Figure 18: Total Concentration Contours of Chemical Components (in [mol L$^{-1}$]) for the Case ELEVATED-SULPHATE at 3.25×10$^4$ Years. The White Rectangle in (g) Indicates the Data Extraction Region (i.e. Horizontal from 250 to 420 km and Vertical from 3000 to 4000 m) for HS$^-$ Concentrations Shown in Figure 19**

Comparison of the simulated vertical profiles in the data extraction region (area contained within the white rectangle in Figure 18(g)) to observed sulphide concentrations shows good agreement, similar to the case BASE. The highest average HS$^-$ concentrations show better agreement with the maximum observed data (at approximately 3,900 to 3,850 m) than those from the case BASE.
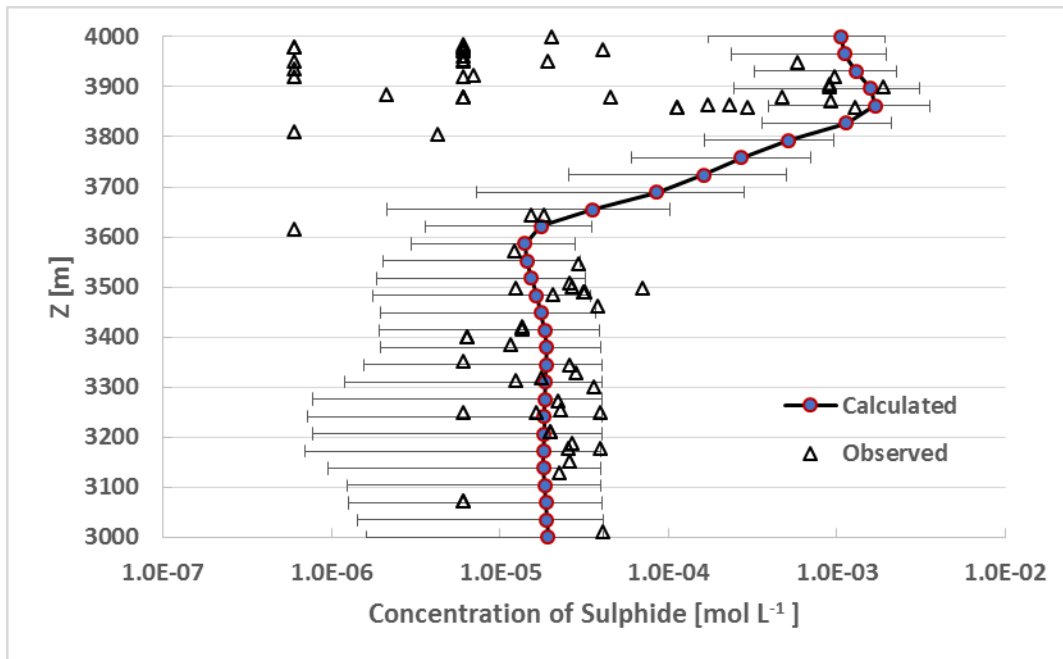
**Figure 19: Comparison of the Observed Sulphide Data and the Simulated Average HS⁻ Concentrations (in [mol L⁻¹]) +/- Standard Deviations (Horizontal Black Lines) at Different Depths for the Region Shown in Figure 18(g). Simulation Results are for the Case ELEVATED-SULPHATE at 3.25×10⁴ Years under Interglacial Conditions; Observed Data are from Carter et al. (2015)**

### 3.4.3 Case OXYGEN-CONSUMPTION

This case is derived from the case BASE by adding the consumption of oxygen via reaction with organic substances. In comparison to the case BASE, dissolved oxygen shows much less downward migration (compare Figure 20(h) to Figure 16(h)). Consequently, the inhibition effect of dissolved oxygen on the biogenic sulphate reduction is decreased. In comparison to the case BASE, the simulated distribution of HS⁻ shows higher total sulphide concentrations in the regions where dissolved oxygen ingress occurs in the case BASE (Figure 16(h)). Otherwise, no visible differences can be observed (compare Figure 20(g) to Figure 16(g)). Comparing Figure 21 to Figure 17, the average concentrations of HS⁻ increased up to 7.5% to depths of 50m from the top boundary. This case demonstrates that the inclusion of oxygen consumption does not have a significant impact on biogenic sulphate reduction for quasi steady-state interglacial conditions. This behavior can be explained by the limited ability of oxygen to enter deeper regions due to the stable flow field, controlled by the presence of highly saline waters below surficial fresh waters, and the regional hydrostratigraphy which favors lateral groundwater flow.
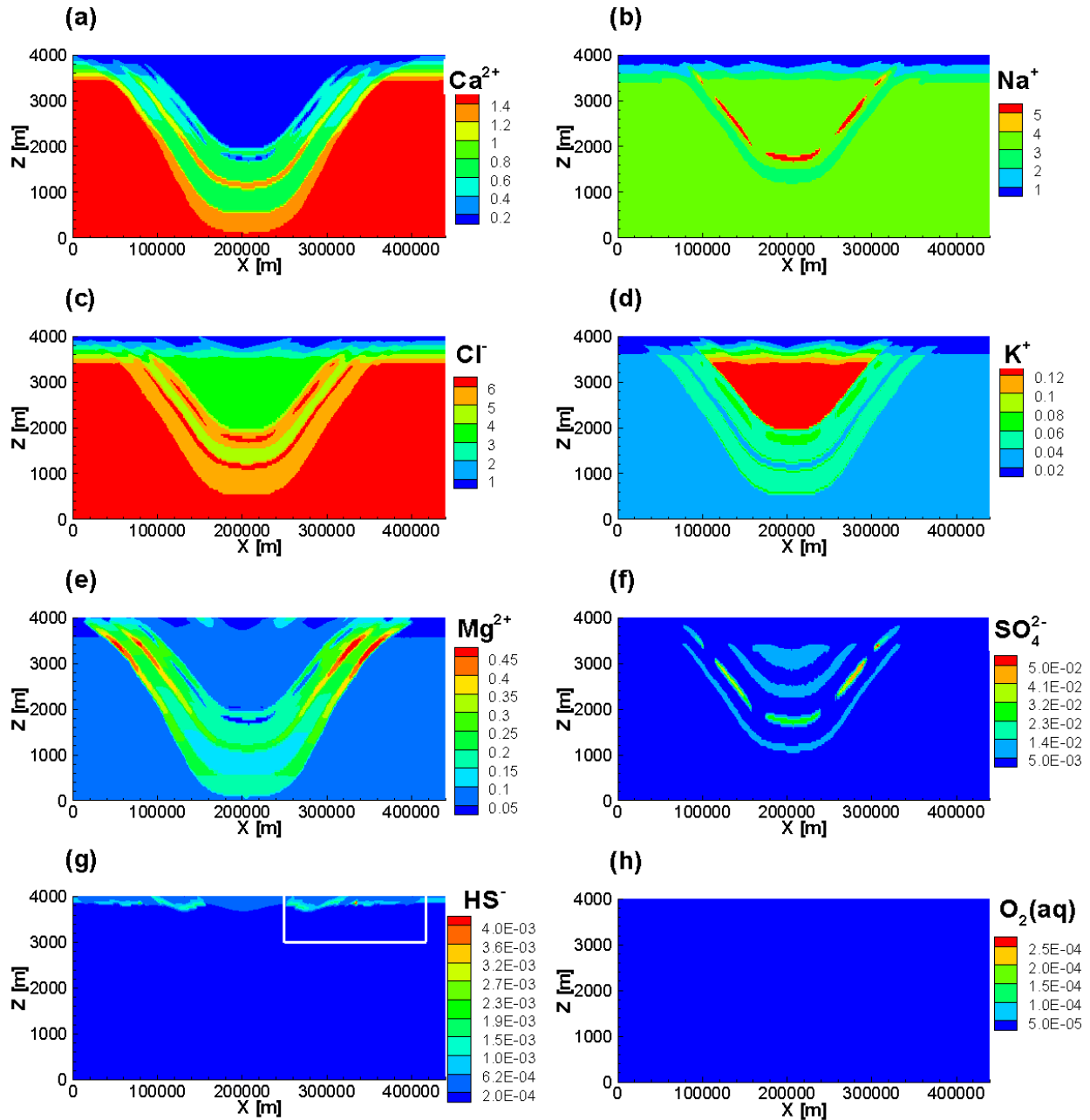
**Figure 20: Total Concentration Contours of Chemical Components (in [mol L$^{-1}$]) for the Case OXYGEN-CONSUMPTION at 3.25×10$^4$ Years. The White Rectangle Indicates the Data Extraction Region (i.e. Horizontal Extension from 250 to 420 km and Vertical Extension from 3000 to 4000 m) for HS$^-$ Concentrations Shown in Figure 21**
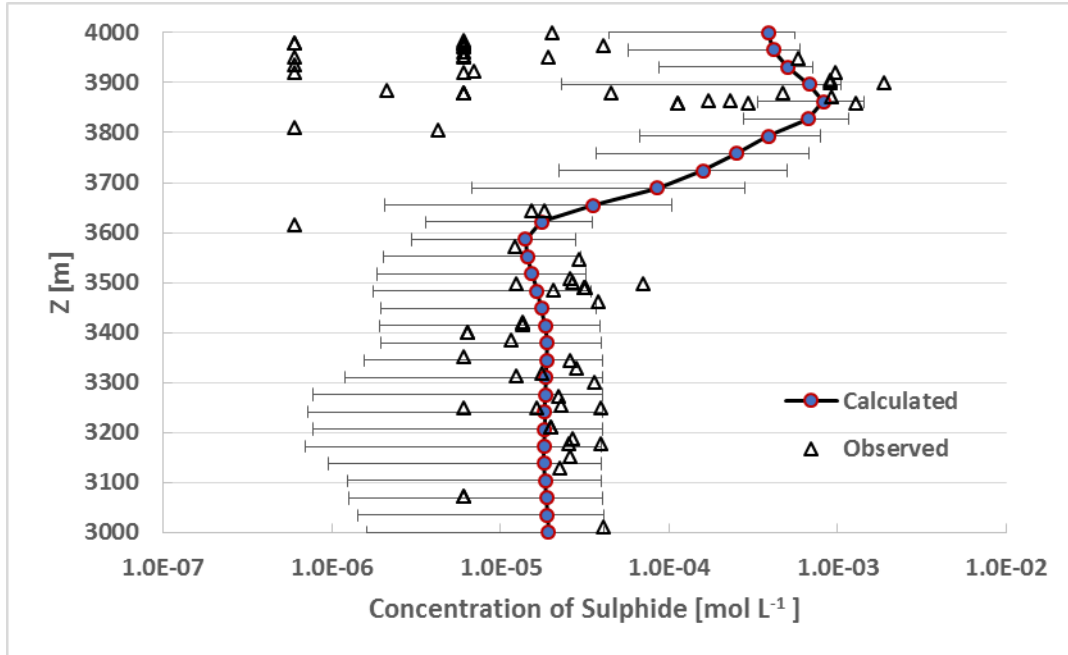
**Figure 21: Comparison of the Observed Sulphide Data and the Simulated Average HS⁻ Concentrations (in [mol L⁻¹]) +/- Standard Deviations (Horizontal Black Lines) at Different Depths for the Region Shown in Figure 20(g). Simulation Results are for the Case OXYGEN-CONSUMPTION at 3.25×10⁴ Years under Interglacial Conditions; Observed Data are from Carter et al. (2015)**

## 3.5 SIMULATION RESULTS – GLACIATION/DEGLACIATION SCENARIO

To investigate the possible effects of glaciation/deglaciation on the formation of sulphidic waters, three cases were simulated – the cases BASE, ELEVATED-SULPHATE and OXYGEN-CONSUMPTION. The initial conditions for these cases were the hydraulic, thermal and geochemical results obtained after $3.25 \times 10^4$ years of the inter-glacial simulations described above.

### 3.5.1 Case BASE

During Stage I the recharge to the basin progressively decreases (Figure 22) as more of the ground surface becomes covered by ice. However, discharge from the basin takes place in front of the toe of the ice sheet due to hydromechanical loading. Discharge continues until complete ice coverage is achieved at 12,500 years. During Stage II (complete ice coverage) the basin is a closed system (Figure 22). This condition arises because of the assumptions inherent to the conceptual model: i.e. a two-dimensional basin, complete ice coverage during glacial maximum, and cold-based conditions.

Results for Stage III are presented at two simulation times, 18,000 years and 20,000 years (see Figure 23), in order to better visualize processes during the period of rapid glacial retreat and high subglacial hydraulic heads. These high hydraulic heads cause relatively large recharge and discharge fluxes during the period of glacial retreat (Figure 22). Near the beginning of Stage III (i.e. 18,000 years), pressure heads increase in shallow permeable units as a consequence of the re-established hydraulic connection between the now warm-based

melting ice sheet and these sedimentary units.  By 20,000 years, the ice sheet has retreated past the center of the basin and the point pressure heads exhibit a general decline at this location.

During Stage IV (i.e. inter-glacial period), the recharge and discharge from the basin are again balanced and pressure heads and solution densities have stabilized close to those assigned as initial conditions (Figure 22 and Figure 23).

Fluid density, salinity and chloride concentrations change significantly during the period of deglaciation (Figure 23 and Figure 25).  After 20,000 years, the retreating ice sheet has passed the central region of the basin, establishing an imbalanced hydraulic boundary condition that drives groundwater flow along the layers with higher hydraulic conductivity towards the left side and results in a region with lower density fluids up to a depth of around 350 m.  However, during Stage IV, after the ice sheet has completely disappeared, the hydraulic boundary conditions return to the same conditions as for the initial stage.  The composition of formation waters return to concentration distributions similar to those present during prior interglacial conditions.

During Stages I and II, concentration distributions of chemical components remain almost constant.  At 20,000 years, the concentration of major ions such as $Cl^-$ and $SO_4^{2-}$ are low in the region with low fluid density, while concentrations of dissolved oxygen are more elevated (Figure 24 and Figure 25).  Low sulphate in these regions limits the formation of sulphide during these periods; however, some sulphate is supplied by diffusion, local mixing and dissolution of anhydrite in this region.  Inhibition of biogenic sulphate reduction is short lived.  After complete deglaciation (from 22,500 years on), sulphide concentrations in the region replaced by melting water accumulate with time (Figure 25).  During the post-glaciation stage, the geochemical system adapts slowly and at 50,000 years, the $Cl^-$ and $HS^-$ concentration distributions (Figure 26) is approaching those at 32,500 years in the case BASE for the inter-glaciation scenario (compare Figure 26 to Figure 16(c) and (g)).  This indicates that the hydrogeochemical system is able to re-establish a quasi-stable equilibrium state following the glacial perturbation.
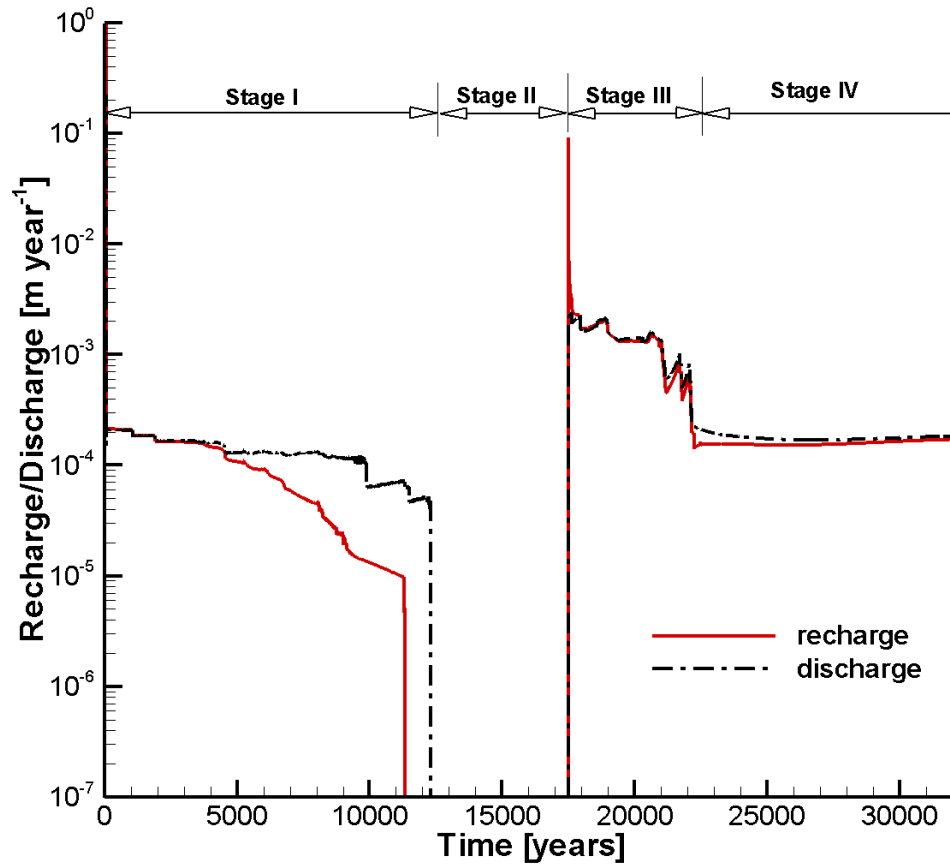
**Figure 22: Simulated Temporal Evolution of Recharge and Discharge for the Case BASE – Glaciation/Deglaciation Scenario**
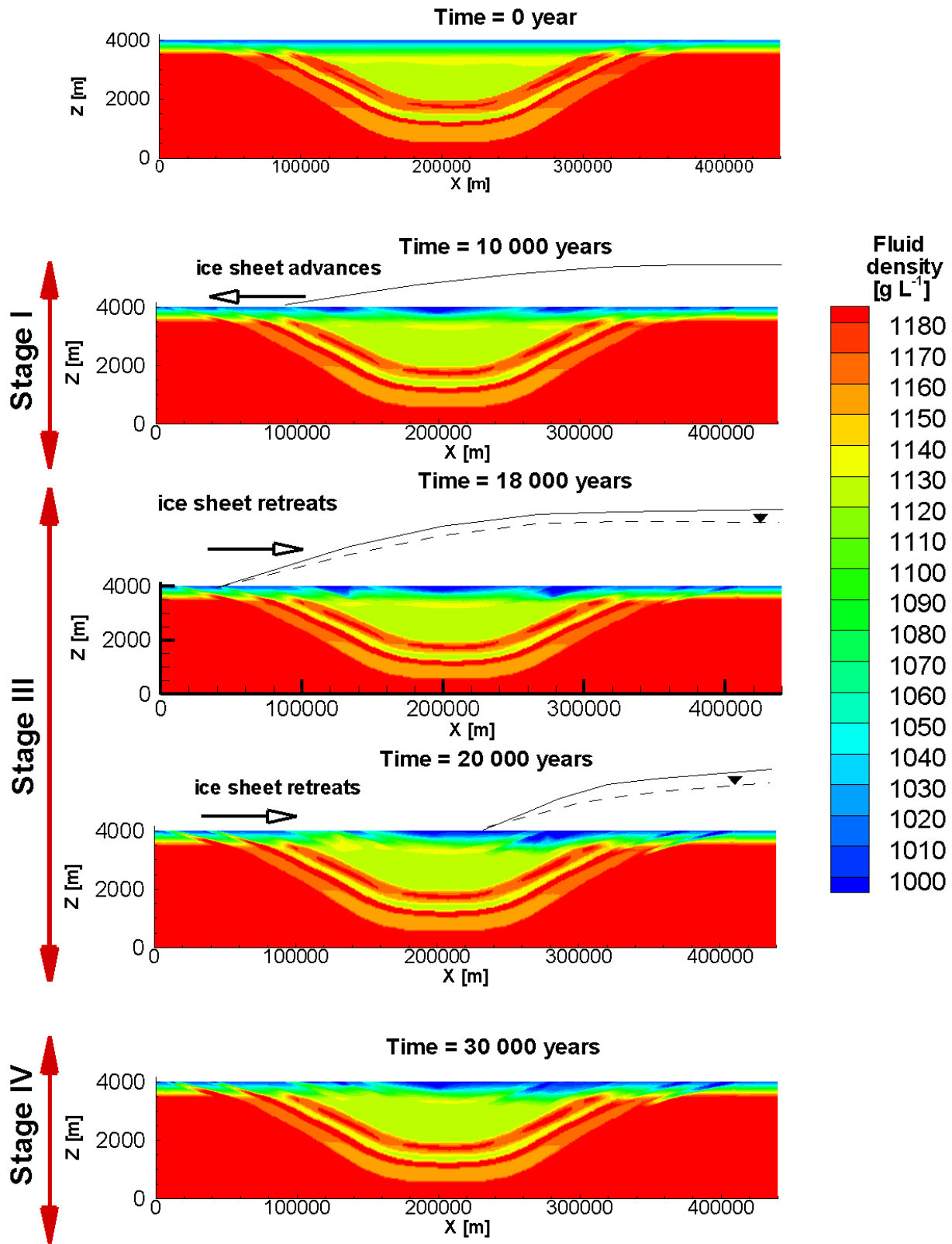
**Figure 23: Simulated Liquid Phase Density for the Case BASE – Glaciation/Deglaciation Scenario**
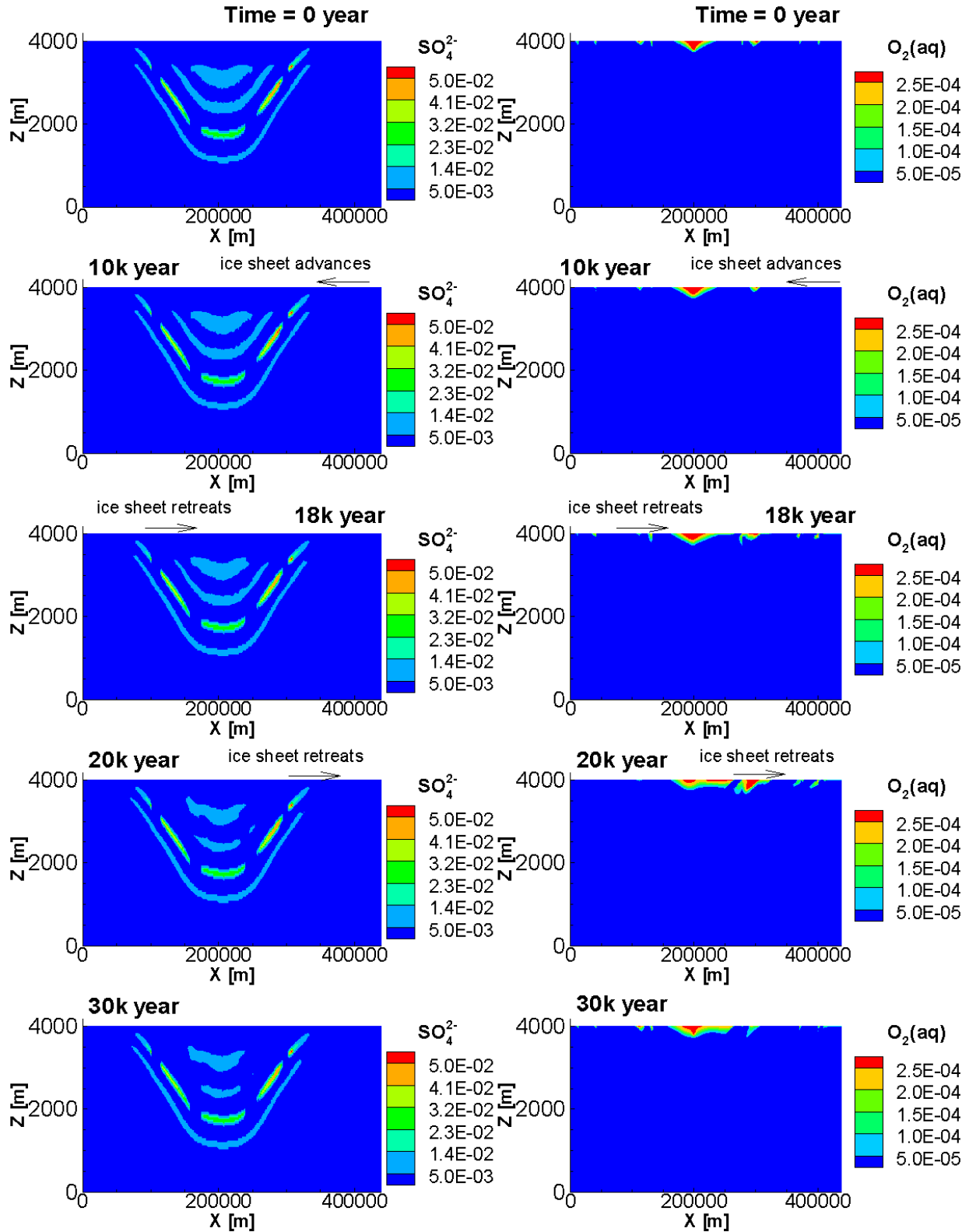
**Figure 24: Simulated Contours of SO$_4$$^{2-}$ and Dissolved O$_2$(aq) Concentrations (in [mol L$^{-1}$]) for the Case BASE – Glaciation/Deglaciation Scenario**
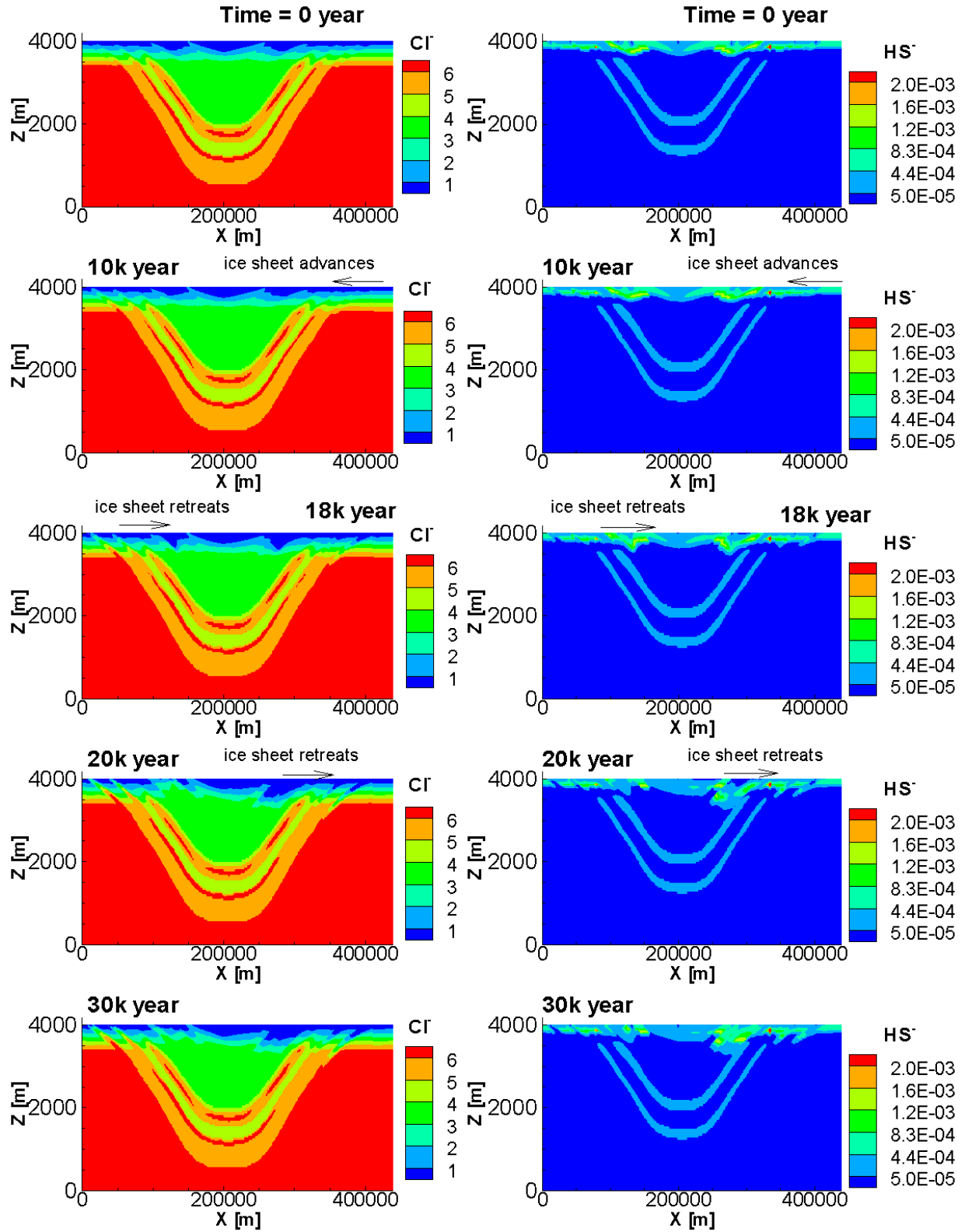
**Figure 25: Simulated Contours of Cl⁻ and HS⁻ Concentrations (in [mol L⁻¹]) for the Case BASE – Glaciation/Deglaciation Scenario**
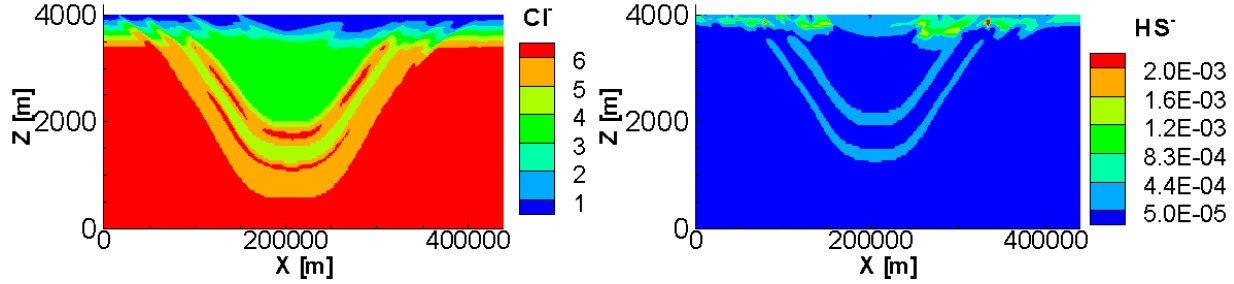
**Figure 26: Concentration Contours of Cl⁻ (left) and HS⁻ (right) (in [mol L⁻¹]) for the case BASE at 50,000 Years**

### 3.5.2 Case ELEVATED-SULPHATE

Similar to the case BASE, the simulated concentration profiles for the case ELEVATED-SULPHATE show significant replacement of the formation fluid by meltwater during Stage III (Figure 27 and Figure 28). Higher initial concentrations of sulphate (see Figure 15) near the top boundary allow biogenic sulphate reduction to proceed, resulting in a larger area with higher sulphide concentrations near the left and right top boundaries in comparison to the case BASE (compare Figure 28 to Figure 25). During glacial retreat groundwater with elevated sulphide concentrations, present in the more permeable sandstones, is pushed downwards. Sulfide concentrations in regions with low fluid density and salinity, resulting from the ingress of meltwater, increase again during Stage IV. Nevertheless, as for the other simulations, sulphidic waters occur only in regions close to the ground surface. Regions affected by the ingress of meltwater slowly recover after completion of the glaciation/deglaciation cycle, and the maximum depth of sulphide generation decreases with time as a result of increasing salinity, as the flow systems returns to quasi steady-state conditions present during interglacial periods.
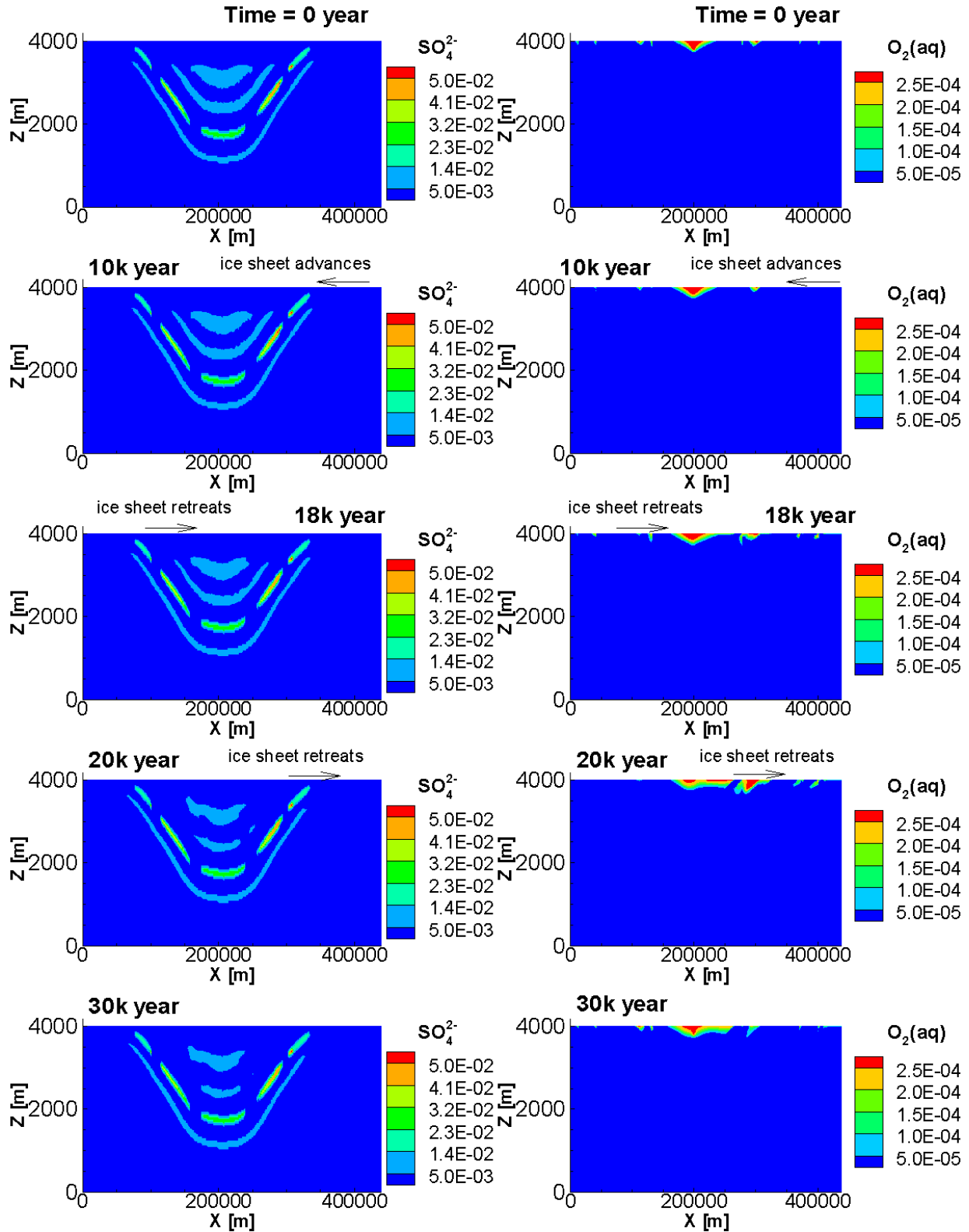
**Figure 27: Simulated Concentration (in [mol L$^{-1}$]) Contours of SO$_4^{2-}$ (Left) and Dissolved O$_2$(aq) for the Case ELEVATED-SULPHATE – Glaciation/Deglaciation Scenario**
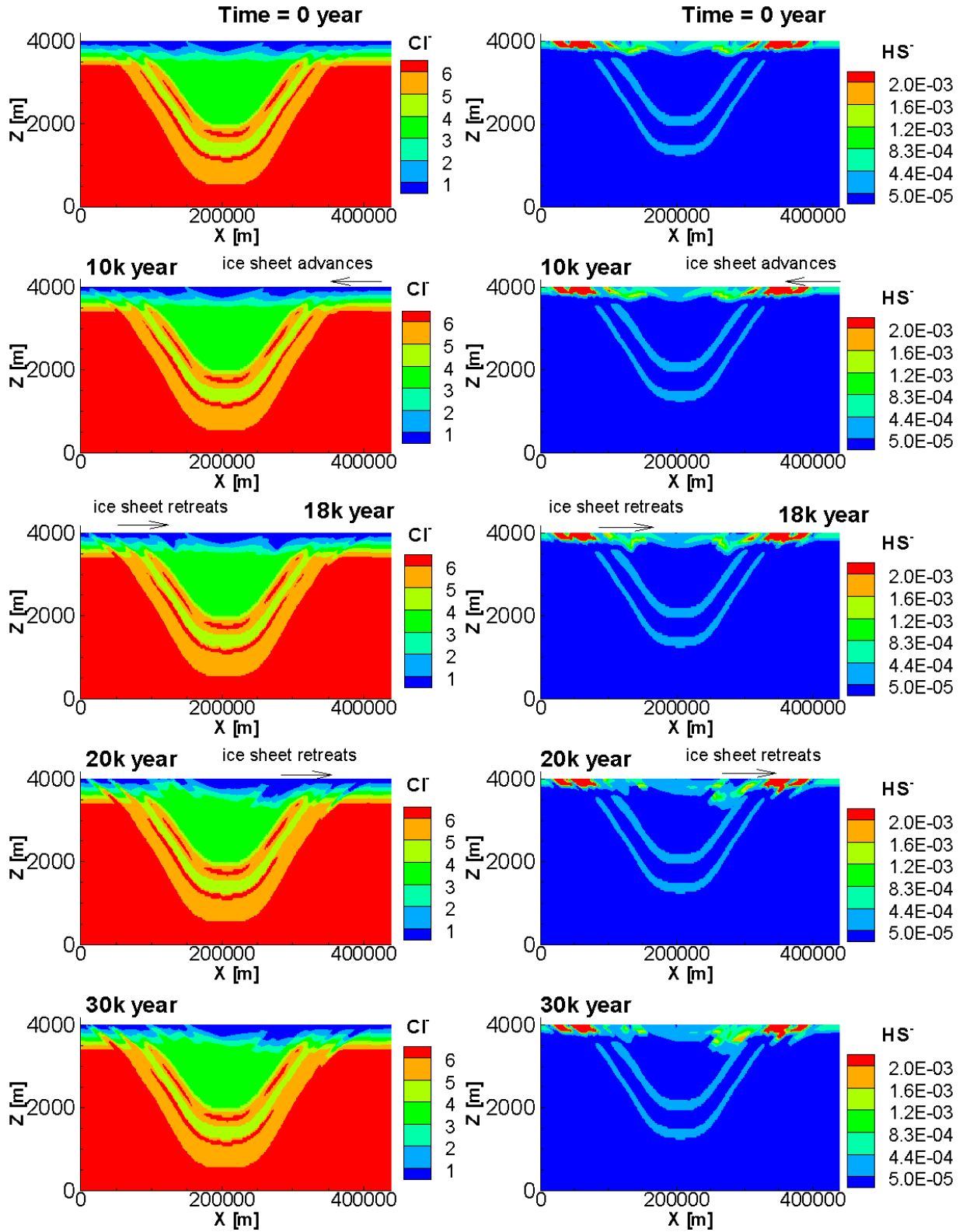
**Figure 28: Simulated Contours of Cl⁻ and HS⁻ Concentrations (in [mol L⁻¹]) for the Case ELEVATED-SULPHATE – Glaciation/Deglaciation Scenario**

### 3.5.3 Case OXYGEN-CONSUMPTION

Simulated results for the case OXYGEN-CONSUMPTION are depicted in Figure 29 and Figure 30 and show significant differences in dissolved $O_2$(aq), resulting locally in moderately increased sulphide concentrations, in comparison to the case BASE (Figure 25 and Figure 24). Dissolved $O_2$(aq) concentrations are more depleted within the top 200 m due to oxygen consumption via the oxidation of organic matter. Consequently, the inhibition effect of $O_2$(aq) on biogenic sulphate reduction is decreased. During stage I, the ice sheet advancement is assumed to be cold-based, which prevents downward seepage and thus recharge of dissolved oxygen. Consequently, the dissolved oxygen in the subsurface is consumed, allowing biogenic sulphate reduction to proceed (see 10,000 years in Figure 30 right). When the ice sheet retreats, glacial meltwater recharge results in a higher $O_2$(aq) concentration in the groundwater near the top boundary (see 18,000 years in Figure 30 right). At 20,000 years, the ice sheet retreats past the center point, leaving the left part of the domain as a discharge area. At 30,000 years, i.e. 7,500 years after complete glacial retreat, the $O_2$(aq) concentration distribution is approaching the initial condition. At 30,000 years the maximum concentration of dissolved $O_2$(aq) is three orders of magnitude lower in comparison to that in case BASE (Figure 31 top).

In the case BASE, $O_2$(aq) penetrates preferentially along layers with relatively higher hydraulic conductivities and with higher vertical hydraulic gradients (e.g. the area around x=200 km near the top boundary). In the case OXYGEN-CONSUMPTION, $O_2$(aq) penetrates in the same manner as in the case BASE; however, a large fraction of $O_2$(aq) is consumed in the current case, resulting in much lower concentrations of $O_2$(aq) in the same areas showing preferential penetration in the case BASE. As a result, $HS^-$ concentrations are higher by up to one order of magnitude for the case OXYGEN-CONSUMPTION in comparison to the case BASE (Figure 31 bottom), especially in the zones affected by $O_2$(aq) ingress.
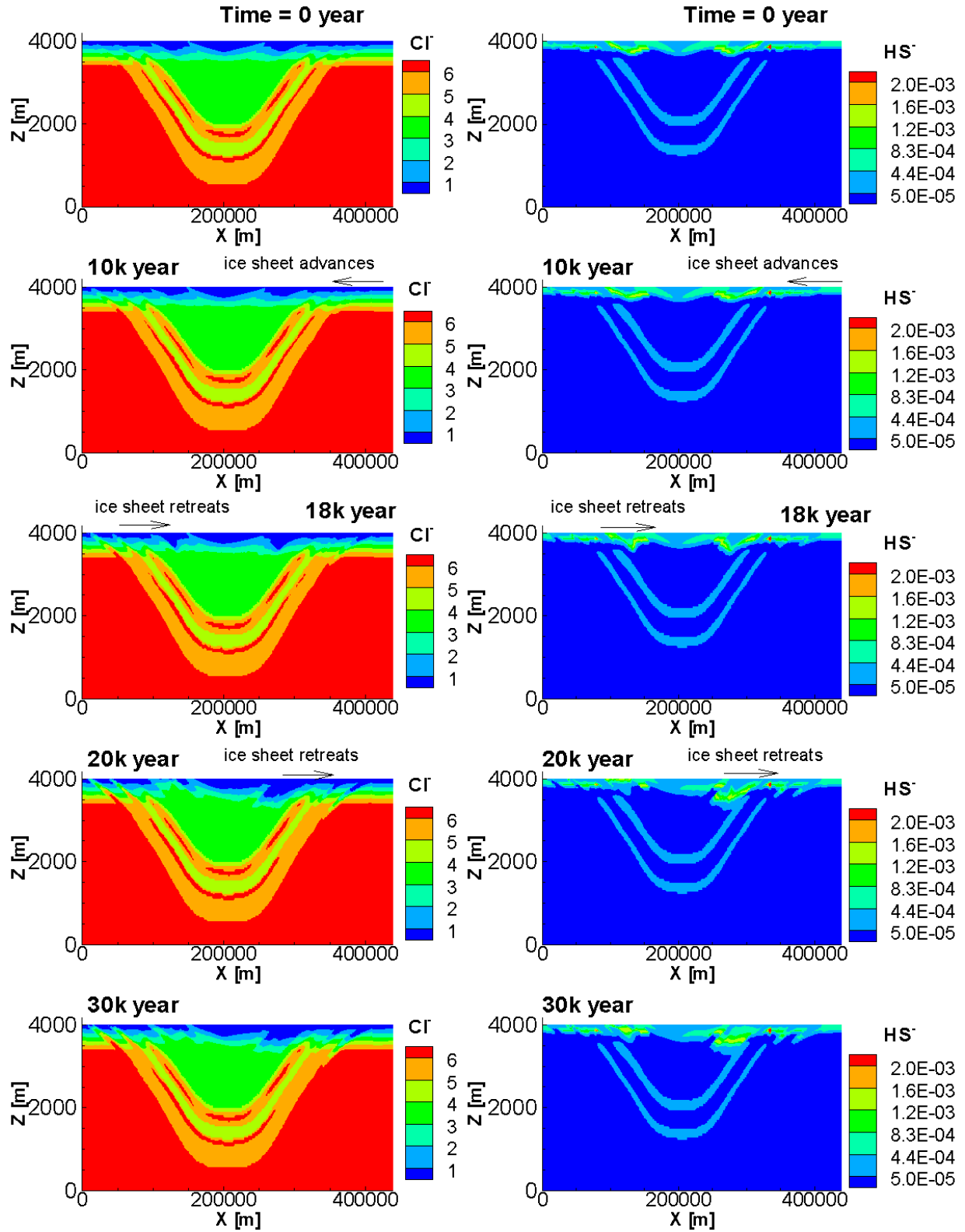
**Figure 29: Simulated Contours of Cl⁻ and HS⁻ Concentrations (in [mol L⁻¹]) for the Case OXYGEN-CONSUMPTION – Glaciation/Deglaciation Scenario**
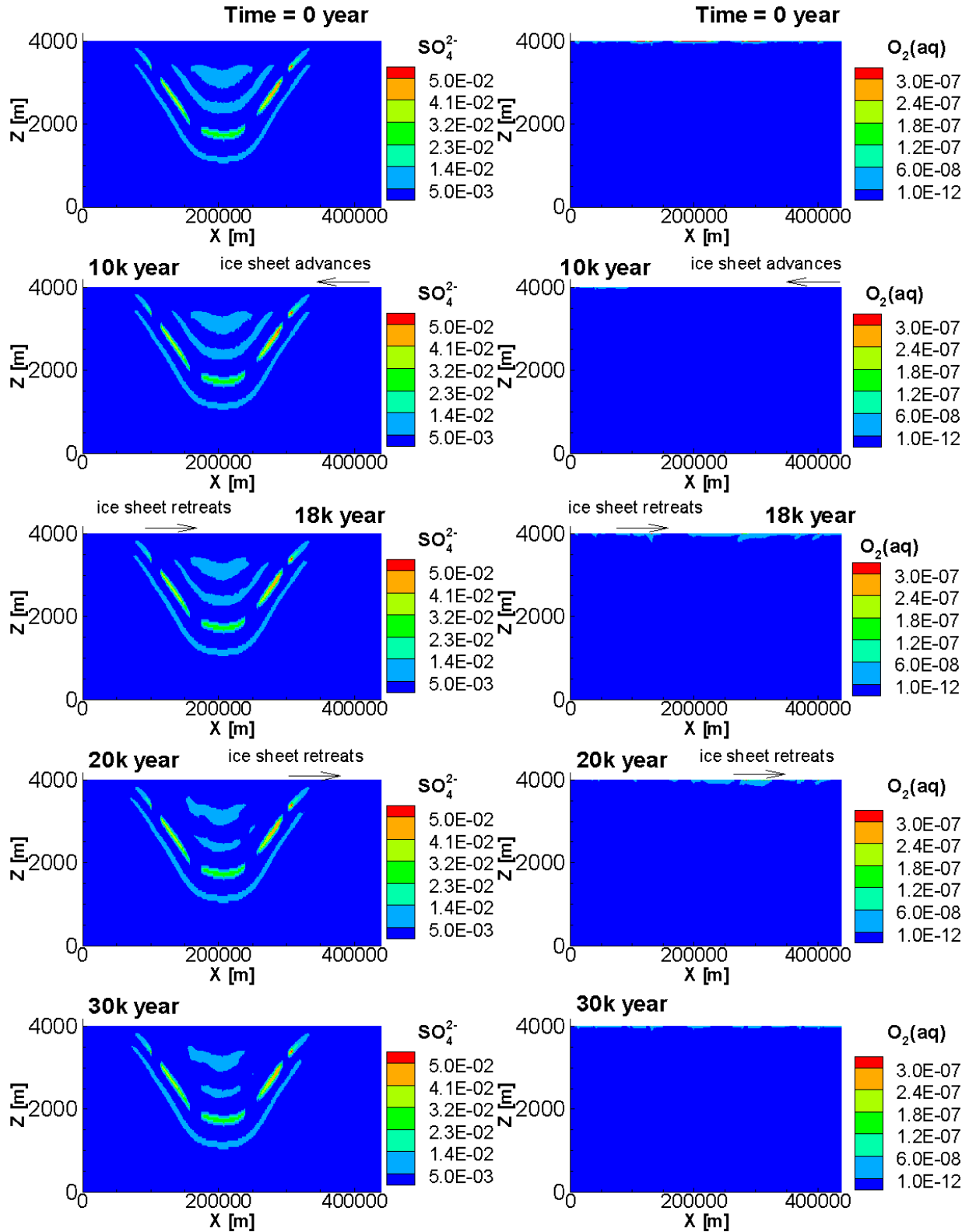
**Figure 30: Simulated Contours of SO₄²⁻ and O₂(aq) Concentrations (in mol L⁻¹) for the Case OXYGEN-CONSUMPTION – Glaciation/Deglaciation Scenario**
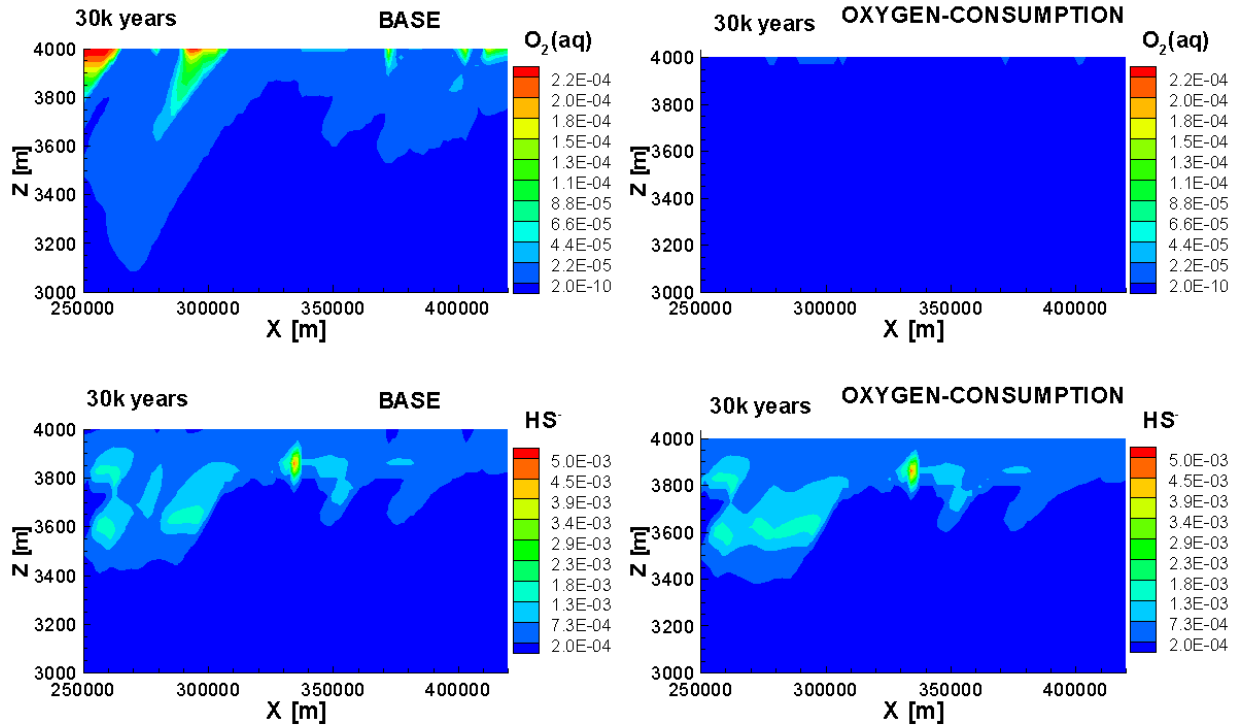
**Figure 31: Comparison of Concentration (in [mol L$^{-1}$]) Contours of O$_2$(aq) and HS$^-$ for Case BASE (Left) and Case OXYGEN-CONSUMPTION (Right) for the Selected Region Shown in Figure 18(g) – Glaciation/Deglaciation Scenario**

## 4. DISCUSSION AND CONCLUSIONS

Sulphidic groundwaters that have been identified at intermediate depths (approximately 100 to 200 m) in the Michigan Basin sedimentary rocks of southern Ontario have been attributed to biogenic sulphate reduction. The activity of sulphate reducing bacteria (SRB) is highly dependent on the geochemical properties of the fluid especially the concentration of sulphate, redox conditions and salinity. High salinity can strongly suppress biogenic sulphate reduction. A simplified model for sulphate reduction, which considers the inhibitory effect of high salinity, has been developed and implemented in MIN3P-THCm and was verified against PHREEQC. The model results for sulphate reduction in highly saline conditions have not been compared to data from controlled experiments as such data sets were not identified.

The model was applied to investigate the formation of sulphidic waters for a 2D generic basin scale model. Two scenarios were investigated: inter-glacial conditions, and transient conditions during a single glaciation/deglaciation cycle. Simulations based on interglacial conditions were conducted to investigate factors controlling the formation of sulphidic waters during quasi steady-state, present-day conditions. The simulations involving a glaciation/deglaciation cycle were performed to investigate impacts associated with the advancement and retreat of an ice sheet on the formation of sulphidic waters.

Inter-glacial simulations illustrate how high salinity strongly suppresses biogenic sulphate reduction. In addition, the simulations show how limited sulphate availability and the presence of dissolved oxygen inhibit progress of this reaction. The consumption of dissolved oxygen via organic matter oxidation resulting in lower concentrations of $O_2$(aq) was limited near the top boundary of the domain up to a depth of about 50 m, especially along rocks with relatively higher hydraulic conductivities, and therefore diminishes the inhibition effect of $O_2$(aq) on biogenic sulphate reduction locally. In all simulation cases, the highest concentrations of total sulphide occurred around depths of 150 m. The simulations indicate that significant concentrations of sulphide are only produced to depths of approximately 200 m, which generally agrees with the observed distribution of data presented by Carter et al. (2015).

The simulations suggest that a glaciation/deglaciation cycle can have significant, but relatively short term, impacts on the maximum depth of sulphidic water occurrence. The most significant effects are seen during glacial retreat when substantial volumes of meltwater push sulphide-containing formation water to depths of up to 350 m. However, this process is restricted to layers with higher permeability, namely the sandstone units. In addition, lower salinity at depth provides more favorable conditions for biogenic sulphate reducing bacteria, but only if sufficient concentrations of sulphate become available. In the simulations, sulphate is supplied by diffusion from regions containing elevated sulphate concentrations and/or dissolution of anhydrite. In the long term, the hydrogeochemical system is able to re-establish the pre-existing equilibrium state after glacial perturbation.

**ACKNOWLEDGEMENTS**

**REFERENCES**

Appelo, C. and D. Postma.  2005.  Geochemistry, Groundwater and Pollution. CRC Press; 2 edition.

Bea, S.A., J. Carrera, J.M. Soler, C. Ayora and M.W. Saaltink.  2004.  Simulation of remediation alternatives for a $^{137}$Cs contaminated soil.  Radiochimica Acta, 92, 827-833.

Bea, S.A., K.U. Mayer and K.T.B. MacQuarrie.  2011.  Modelling Reactive Transport in Sedimentary Rock Environments - Phase II MIN3P code enhancements and illustrative simulations for a glaciation scenario.  Nuclear Waste Management Organization Technical  Report NWMO TR-2011-13.

Bea, S.A., K.U. Mayer and K.T.B. MacQuarrie.  2012.  Modelling of reactive transport in a hypothetical sedimentary basin affected by a glaciation/deglaciation event. 39th IAH Congress, Niagara Falls, Canada: September 16-21.

Bea, S.A., K.U. Mayer and K.T.B. MacQuarrie.  2016.  Reactive transport and thermo-hydro-mechanical coupling in deep sedimentary basins affected by glaciation cycles: model development, verification, and illustrative example, Geofluids, 16, 279–300.

Bense, V.F. and M.A. Person.  2008.  Transient hydrodynamics within intercratonic sedimentary basins during glacial cycles. Journal of Geophysical Research-Earth Surface, 113, Article No. F04005, 1-17.

Brandt, K., F. Vester, A.N. Jensen and K. Ingvorsen.  2001.  Sulfate reduction dynamics and enumeration of sulfate-reducing bacteria in hypersaline sediments of the Great Salt Lake (Utah, USA).  Microbial Ecology, 41(1), 1-11.

Brown, K. A.  1982.  Sulphur in the environment: a review.  Environmental Pollution Series B, Chemical and Physical, 3(1), 47-80.

Carter, T.R.  2012.  Regional groundwater systems in southern Ontario.  Ontario Oil & Gas: 44-48.

Carter, T.R., D. Wang, A. Castillo and L. Fortner.  2015.  Water type maps of deep groundwater from petroleum well records, southern Ontario.  Ontario Oil, Gas & Salt Resources Library, Open file data release 2015-1.

Foti M., D.Y. Sorokin, B. Lomans, M. Mussman, E.E. Zakharova, N.V. Pimenov, J.G. Kuenen and G. Muyzer.  2007.  Diversity, activity and abundance of sulfate-reducing bacteria in saline and hypersaline soda lakes.  Applied and Environmental Microbiology, 73, 2093–2100.

Giambalvo, E.R., C.I. Steefel, A.T. Fisher, N.D. Rosenberg and C.G. Wheat.  2002.  Effect of fluid-sediment reaction on hydrothermal fluxes of major elements, eastern flank of the Juan de Fuca Ridge. Geochim. Cosmochim. Acta, 66 (10), 1739–1757.

Gibson, B., R.T. Amos and D.W. Blowes. 2011. 34S/32S fractionation during sulfate reduction in groundwater treatment systems: Reactive transport modeling. Environmental Science & Technolog,y 45, 2863–2870.

Hanor, J. 1987. Origin and migration of subsurface sedimentary brines. Soc. Sediment. Geol. Short Course 21, Soc. of Econ. Paleontol. and Mineral., Tulsa, Okla.

Harvie, C.E., N. Moller and J.H. Weare. 1984. The prediction of mineral solubilities in natural waters: The $Na-K-Mg-Ca-H-Cl-SO_4-OH-HCO_3-CO_3-CO_2-H_2O$ system to high ionic strengths at $25^oC$. Geochimica et Cosmochimica Acta, 48, 723-751.

Henderson, T., K.U. Mayer, B. Parker and T. Al. 2009. Three-dimensional density-dependent flow and multicomponent reactive transport modeling of chlorinated solvent oxidation by potassium permanganate. Journal of Contaminant Hydrology, 106, 195-211.

Hobbs, M.Y., S.K. Frape, O. Shouakar-Stash and L.R. Kennell. 2011. Regional Hydrogeochemistry -Southern Ontario. Nuclear Waste Management Organization Report NWMO DGR-TR-2011-12 R000. Toronto, Canada.

INTERA Engineering. 2011. Descriptive Geosphere Site Model. Intera (Geofirma) Engineering Ltd. report for the Nuclear Waste Management Organization NWMO DGR-TR-2011-24. Toronto, Canada.

Littlewood, D. and J.R. Postgate. 1957. Sodium chloride and the growth of Desulphovibrio desuplphuricans. Journal of general microbiology, 17(2), 378–389.

MacInnes, D.A. 1919. The activities of the ions of strong electrolytes: Journal American Chemical Society, 41, 1086-1092.

Mayer, K.U. 1999. A numerical model for multicomponent reactive transport in variably-saturated porous media, PH.D. – thesis, Department of Earthe Sciences, University of Waterloo, Waterloo, Ontario, Canada.

Mayer, K.U., S.G. Benner, E.O. Frind, S.F. Thornton and D.L. Lerner, 2001. Reactive transport modeling of processes controlling the distribution and natural attenuation of phenolic compounds in a deep sandstone aquifer, Journal of Contaminant Hydrology, 53, 341-368

Mayer, K.U., E.O. Frind and D.W. Blowes. 2002. Multicomponent reactive transport modeling in variably saturated porous media using a generalized formulation for kinetically controlled reactions. Water Resources Research, 38, 1174. doi:10:1029/2001WR000862

Mayer, K.U. and K.T.B. MacQuarrie. 2010. Solution of the MoMaS reactive transport benchmark with MIN3P- model formulation and simulation results, Computational Geosciences, 14, 405-419.

McIntosh, J.C. and L.M. Walter. 2005. Volumetrically significant recharge of Pleistocene glacial meltwaters into epicratonic basins: Constraints imposed by solute mass balances. Chemical Geology, 222, 292-309.

Medina, C.R., J.A. Rupp and D.A. Barnes. 2011. Effects of reduction in porosity and permeability with depth on storage capacity and injectivity in deep saline aquifers: A case study from the Mount Simon Sandstone aquifer. International Journal of Greenhouse Gas Control, 5, 146-156.

Middelburg, J.J. 1989. A simple rate model for organic matter decomposition in marine sediments. Geochimica et Cosmochimica Acta, 53(7):1577-1581

OME (Ontario Ministry of the Environment). 2006. Technical Support Document for Ontario Drinking Water Standards, Objectives and Guidelines, PIBS 4449e01.

Oren, A. 1999. Bioenergetic aspects of halophilism. Microbiology and Molecular Biology Reviews 63:334–348

Parkhurst, D.L. and C.A.J. Appelo 2013. Description of input and examples for PHREEQC version 3 − A computer program for speciation, batch-reaction, one-dimensional transport, and inverse geochemical calculations: U.S. Geological Survey Techniques and Methods, book 6, chap. A43, 497 p. http://pubs.usgs.gov/tm/06/a43/.

Pfister M., N. E. Martin, L.P. Haskell and J.S. Barrett. 2004. Optimizing dose selection with modeling and simulation: application to the vasopeptidase inhibitor M100240. Journal of Clinical Pharmacology. 44:621–631. doi: 10.1177/0091270004265365.

Post, V., H. Kooi and C. Simmons. 2007. Using hydraulic head measurements in variable-density ground water flow analyses. Ground Water, 45, 664-671.

Tang, K., V. Baskaran and M. Nemati. 2009. Bacteria of the sulphur cycle: an overview of microbiology, biokinetics and their role in petroleum and mining industries. Biochemical Engineering Journal, 44(1), 73-94.

Wolery, T. and R. Jarek. 2003. Software user's manual. EQ3/6, Version 8.0. Sandia National Laboratories. U.S. Department of Energy Report.

Xie, M., P. Rasouli, K.U. Mayer and K.T.B. MacQuarrie. 2014a. Reactive Transport Modelling of In-situ Diffusion Experiments for the Mont Terri Project − MIN3P-THCm Code Enhancement and Numerical Simulations, Nuclear Waste Management Organization Technical Report NWMO-TR-2014-25.

Xie, M., P. Rasouli, K.U. Mayer and K.T.B. MacQuarrie. 2014b. Reactive Transport Modelling in Low Permeability Media – MIN3P-THCm Simulations of EBS TF-C Compacted Bentonite Diffusion Experiments, Nuclear Waste Management Organization Technical Report NWMO-TR-2014-23.